ELIMINATION OF CATASTROPHIC OPTICAL MIRROR DAMAGE IN HIGH-POWER LASER DIODES USING MULTI-SECTION WAVEGUIDES

A THESIS SUBMITTED TO
THE GRADUATE SCHOOL OF ENGINEERING AND SCIENCE
OF BILKENT UNIVERSITY
IN PARTIAL FULFILLMENT OF THE REQUIREMENTS FOR
THE DEGREE OF
MASTER OF SCIENCE
IN
MATERIAL SCIENCE AND NANOTECHNOLOGY

By
Kaveh Ebadi
August 2022

Elimination of catastrophic optical mirror damage in high-power laser diodes using multi-section waveguides
By Kaveh Ebadi
August 2022

We certify that we have read this thesis and that in our opinion it is fully adequate, in scope and in quality, as a thesis for the degree of Master of Science.

Abdullah Demir(Advisor)

Hasan Yilmaz

Parviz Elahi

Approved for the Graduate School of Engineering and Science:

rhan Arıkan
Director of the ~~Graduate~~ School

ABSTRACT

ELIMINATION OF CATASTROPHIC OPTICAL MIRROR DAMAGE IN HIGH-POWER LASER DIODES USING MULTI-SECTION WAVEGUIDES

Kaveh Ebadi
M.S. in MATERIAL SCIENCE AND NANOTECHNOLOGY
Advisor: Abdullah Demir
August 2022

One of the solid constraints of high-power laser diodes (LDs) has been catastrophic optical mirror damage (COMD), restricting the operating power level and lifetime of commercial high-power laser diodes (LDs). The output facet of LD reaches a critical temperature leading to COMD, a permanent device failure. Here, we fabricate multi-section LDs by tailoring the waveguide structure along the cavity that distances the output facet from the heat-generating lasing region. This method splits the LD waveguide into electrically isolated laser and window sections along the cavity. The laser section is operated at a high current to achieve high output power, and the window is biased at a low current with minor heat generation. This technique limits the thermal impact of the laser section on the facet, and the window section enables lossless transport of the laser to the output facet. First, we compared standard broad area laser diode with multi-section waveguide LDs up to the maximum achievable power. While traditional single-section LDs show COMD failures, the multi-section waveguide LDs are COMD-free. Next, we implemented our method on narrow waveguide laser diodes and array lasers with different widths and confirmed the cooling effect on the fabricated LD facet. Therefore, our novel technique and results show that the multi-section waveguide method provides substantial reliability improvement for various LD types, such as broad-area, narrow waveguide, and array/bars.

Keywords: Photonics, semiconductor laser, multi-section waveguide, laser facet cooling, catastrophic optical mirror damage (COMD), thermoreflectance.

ÖZET

YÜKSEK GÜÇLÜ LAZER DIYOTLARDA ÇOK BÖLÜMLÜ DALGA KILAVUZLARI KULLANARAK YIKICI OPTIK AYNA HASARININ ORTADAN KALDIRILMASI

Kaveh Ebadi
Malzeme Bilimi ve Nanoteknoloji, Yüksek Lisans
Tez Danışmanı: Abdullah Demır
Ağustos 2022

Yüksek güçlü lazer diyotlar (LD) için süregelen problemlerden biri, ticari yüksek güçlü LD'lerin çalışma güç seviyesini ve kullanım ömrünü sınırlayan, yıkıcı optik ayna hasarı (COMD) olmuştur. LD'nin yüzeyi kritik bir sıcaklığa ulaşır ve bu da geri dönüşü olmayan bir cihaz hasarı olan COMD'ye neden olur. Bu çalışmada, LD çıkış yüzeyini ısı üreten lazer bölgesinden uzaklaştıran bir dalga kılavuzu yapısı oluşturarak çok bölümlü LD'ler ürettik. Bu yöntem, LD dalga kılavuzunu elektriksel olarak yalıtılmış lazer ve pencere bölümlerine ayırır. Lazer bölümü, yüksek çıkış gücü elde etmek için yüksek akımda akımda çalışırken pencere bölümü ihmal edilebilir ısı üretimi olan düşük bir akımda pompalanır. Bu tasarım lazer bölümünün LD yüzeyi üzerindeki termal etkisini kısıtlar ve pencere bölümü lazer ışığının çıkış yüzeyine kayıpsız taşınmasına izin verir. İlk olarak, standart geniş alanlı LD ile çok bölümlü dalga kılavuzuna sahip LD'leri maksimum ulaşılabilir güce kadar karşılaştırdık. Standart LD'ler COMD arızaları gösterirken, çok bölümlü dalga kılavuzlu yapısındaki LD'lerde COMD hasarı oluşmadığını gözlemledik. Daha sonra, yöntemimizi dar dalga kılavuzlu lazer diyotları ve farklı genişliklere sahip dizin lazerler üzerinde uyguladık ve benzer lazer yüzeyi soğumasını bu lazerlerde de gözlemledik. Bu nedenle, özgün tekniğimiz ve elde ettiğimiz sonuçlar, çok bölümlü dalga kılavuzu yönteminin geniş alan, dar dalga kılavuzu ve dizin/bar gibi çeşitli LD türleri için önemli güvenilirlik geliştirmesi sağladığını göstermektedir.

Anahtar sözcükler: *Fotonik, yarı iletken lazer, çok kovuklu lazer, lazer çıkış yüzeyi soğuması, yıkıcı optik ayna hasarı (COMD), ısıl yansıma.*

Acknowledgement

First of all, I would like to thank my advisor Asst. Prof. Abdullah Demir for his support and fantastic guidance and support helping me to develop my knowledge and skills. I am grateful to Asst. Prof. Hasan Yılmaz and Asst. Prof. Parviz Elahi for reviewing this thesis work and for their valuable feedback.

I want to thank all my friends, colleagues, and members of the Nanophotonic Devices Laboratory (nanoPhD Lab), Serdar Şengül, Abdulmalik Abdulkadir Madigawa, Enes Şeker, Dr. Khalil Dadashi, Turgay Bebek, Doğukan Apaydın, Ali Kaan Sünnetcioğlu, Dr. Babak Olyaeefar, Burak Unal ,Osama Aadil Saadi, and Muhammad Sultani for making my stay here an exciting one. It has been a pleasure to share numerous great recollections with you all. I would like to thank Serdar Şengül for his support in the characterization lab and for helping me in my early days. Also, I would like to thank Enes Şeker for his clean room coaching and for sharing his clean room experience, which has helped me learn faster. Additionally, I wish to acknowledge the UNAM cleanroom staff; Taha Ilıkkan, Abdullah Kafadenk, Murat Gure, and Can Güven, for their help and support in the clean room.

I would like to express my deepest gratitude to my mom, Shahin Hoseini, my dad, Eyvaz Ebadi, and my sister and brother for their love and support.

Above all, Special thanks to the love of my life, Parastoo Karami, for supporting me in every step of my life, and I am grateful for your endless love. My life was full of ups and downs, and I couldn't pass them without you. I have no word to qualify you; I adore you so.

To my wife

Contents

List of Figures

List of Tables

Chapter 1

Introduction

1.1 Laser diodes (LDs)

A device that improves the amplitude of an optical field while preserving its phase is called a coherent optical amplifier. Light amplification by stimulated emission of radiation (LASER) is the principle of achieving coherent light amplification, and generating light in lasers. Three elements are needed to create a laser light: an active medium, a pumping mechanism, and an optical feedback mechanism.

Stimulated emission is a process in which an initial photon induces an electron in an upper energy level in an atom to decay into a lower energy level and emit a clone photon like the initial photon having the same properties such as frequency, direction, and polarization as shown in the figure 1.1 (b). Next, these two photons stimulate the emission of two more photons while preserving the properties of the initial photon, and this process continues like this. The emission wavelength of the recombination depends on the band-gap of the active region material [1, 2]. In the thermal equilibrium condition, light is attenuated while transmitting through matter. The reason is the absorption of the photons by a large number of atoms in lower energy levels dominating the less probable stimulated emissions by a low number of atoms in the upper energy level, figure 1.1 (a) [3].

Therefore, to have laser action, there must be more atoms in the upper energy level compared to the lower one, population inversion. To achieve the population inversion, atoms in the lower energy levels need to be excited to the higher energy levels, which demands a source of power called a pump, shown by the red arrow in figure 1.1 (b). The pump energy can be provided optically or electrically. Last but not least is the optical feedback mechanism. Two reflective mirrors on opposite sides of the active medium provide the feedback mechanism to form an optical resonator; this is how photons travel inside the active medium, causing light amplification.

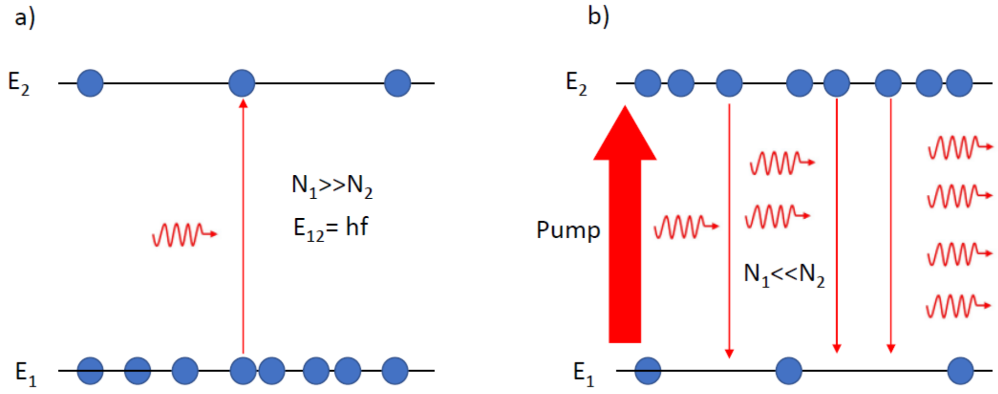

Figure 1.1: (a) Absorption of photons (b) Light amplification by stimulated emission

There are three different features of laser compared to regular light sources:

1. Linewidth: this is a measure of frequencies contained in the emitted light.
2. Coherence: waves of light with a very narrow wavelength range moving in phase with each other in space and time.
3. Directional: compared to other light sources, it has a low divergence angle and is well collimated.

These properties make lasers a suitable light source for many applications ranging from medical imaging to information technology [4].

1.2 Catastrophic optical mirror damage (COMD)

Heat is a fundamental issue for electronic and optoelectronic devices because temperature adversely affects the performance characteristics of almost all devices. Moreover, today, electronic and optoelectronic devices are fabricated at the micro/nanoscale, which puts more pressure on the device performance. Therefore, heat has become a difficulty for sub-micron electronic device development [5]. The deployment of laser diodes (LDs) has increased drastically in the last two decades due to demands in industrial, consumer, and medical applications, among many others [1, 6, 7]. GaAs-based high-power LD has become an established technology for most of these applications. It has the highest electro-optical conversion efficiency among all light sources [8, 9, 10] with record output power levels [11, 12] and high brightness [13, 14]. However, there are factors limiting the output power of LDs, such as carrier leakage, gain saturation that leads to spatial hole burning (SHB), free carrier absorption, catastrophic optical damage (COD) and catastrophic optical mirror damage (COMD) [15, 16, 17]. Among them, the most fundamental issue limiting the output power and reliability is still catastrophic optical mirror damage (COMD) that occurs at the output facet of the laser [18, 19, 20, 21]. It is due to partial absorption of out-coupled emission at the laser facet, which drastically decreases the output power and reliability of the LD. Both the absorption rate at the facet and following heating is a function of laser wavelength, facet coating, and passivation layers properties [22]. Hence, it has been studied extensively. COMD limits the LD's performance and directly affects fiber and solid-state lasers that rely on high-power LDs as pump sources. Studies since the first years agree that the COD mechanism starts when the facet reaches a critical temperature (T_c=120-160 ℃), and it triggers a thermal runaway mechanism as shown in the figure 1.2 that leads to device failure [18]. There are two kinds of feedback loops where one is internal, and the other is an external feedback loop, and both loops increase facet temperature compared to the laser junction temperature.

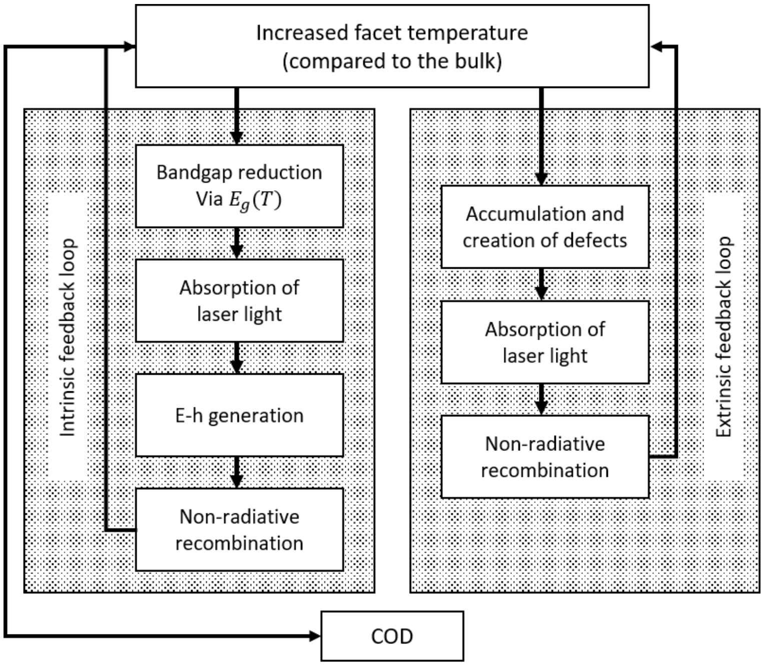

Figure 1.2: Thermal runaway feedback mechanism for COD [14].

This process increases the laser facet temperature and results in micro-explosions on the output facet. This creates the damage that appears as a bump on the laser facet, as shown in figure 1.3 (a), and it extends inside the laser cavity and destroys the device, as shown in figure 1.3 (b). For this reason, a method addressing the COMD in LDs is needed, which directly improves the performance, reliability, and cost of modern high-power LDs and that for fiber and solid-state lasers.

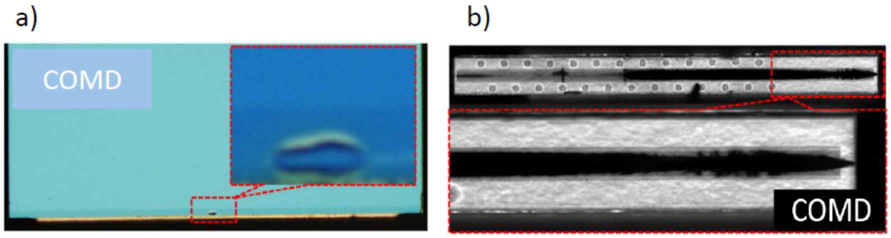

Figure 1.3: (a) Optical microscope image of the laser facet, and (b) Top electro-luminescence (EL) image of the laser cavity.

1.3 Thermal management of LDs

Many successful methods have been reported in the literature to address thermal management in LDs. These approaches can be summarized under two categories: (a) reducing the temperature of the laser device (also referred to as cavity/laser/internal/junction temperature) and (b) increasing the optical strength of the laser output facet. Improving the power conversion efficiency or packaging reduces LD cavity temperature. On the other side, numerous methods have been developed to enhance the optical strength of the laser facet, such as the current blocking layer near the output facet [23] prevents the propagation of electric current towards the laser surface, reducing free carriers, non-absorbing mirror (NAM) [24, 25] structure that reduces the absorption of the output light by shifting or eliminating quantum wells close to the facet, quantum well intermixing [1, 26, 27], passivation of air-exposed surface states [28], and ultra-high vacuum (UHV) passivation [29] that eliminates surface oxidation and reduces the number of point defects. Implementing such approaches mitigate the facet heat sources. Thus, reduced facet temperatures were achieved and resulted in enhanced COMD levels [30, 31]. Even though record high-performance LDs have been demonstrated [8, 9], COMD is still a primary failure mode for commercial high-power LDs. Innovations are desired to obtain COMD-free chips. The attempts described above mainly concentrated on reducing the heat generation by the facet so that the facet temperature is not much higher than the LD cavity [20, 32]. In these approaches, the facet temperature can be made equal to the laser cavity in the ideal case. However, the self-heating of the laser generates a high heat-load, which is the dominant heating source for the laser facet. Effective thermal isolation of such a heat source from the output facet would result in lower facet temperatures [33, 34, 35, 36], which is the method we implemented in this thesis.

1.4 Facet temperature measurement methods

In order to characterize the facet temperature of high-power edge-emitting lasers, many different methods including contact and non-contact modes have been implemented, such as raman spectroscopy [37], infrared (IR) thermography [38, 39], liquid crystal thermography (LCT) technique [38, 39], Fluorescent micro-thermography (FMT) [40, 41], scanning thermal microscopy [42], thermoreflectance and many other techniques as summarized in the table 1.1 [38]. One can get the highest resolution thermal image with approximately 50 nm spatial resolution using scanning thermal microscopy and near-field prob, . However, both methods demand an expensive and complex experimental setup [43] which does not even give a thermal image. Among the techniques providing thermal images, infrared thermography and liquid crystal thermography suffer from low temperature and spatial resolution compared to the thermoreflectance method. On the other hand, thermoreflectance is a non-contact optical measurement technique giving high-resolution thermal images that are useful in many applications such as failure analysis and hot spot detection, temperature distribution mapping, optical characterization, and so on [44]. By implementing this method, quantifying the temperature changes at the laser facet based on measuring the changes in the surface reflectivity is feasible.

Table 1.1: Popular high-resolution thermal measurement techniques in micrometer-nanometer [31].

Method	Principle	Spatial resolution (µm)	Temperature resolution (K)	Response time (s)	Imaging?
Microthermocouple	Seebeck effect	50	0.01	5	No
Infrared thermography	Plank blackbody emission	3-10	1	0.5	Yes
Liquid crystal thermography	Crystal phase transition	2-5	0.5	3	Yes
Thermoreflectance	Temperature dependence of reflection	0.3-0.5	0.01	0.006-0.1	Yes
Scanning thermal microscopy(SThM)	Atomic force microscope with thermocouple or Pt thermistor tip	0.05 surface morphology	0.1	10-100 µs	Scan
Fluorescence thermography	Temperature dependence of quantum efficiency	0.3	0.01	200 µs	Scan
Optical interferometry	Thermal expansion	0.5	0.0001	0.1-0.006	Scan
Micro-Raman	Shift in raman frequency or ratio of Stokes /anti-stokes amplitudes	0.5	1	1 µ	Scan
Near field prob	Use near field to improve optical resolution	0.05	0.1-1	0.1-10 µ	Scan
Built-in temperature sensor	Fabricate a thermal sensor integrated into the device	100	0.0002-0.01	1 µ	No

1.5 Thesis description

Chapter 1 introduces the background on lasers, then describes COMD as the fundamental performance limit in LDs. After that, it presents thermal management techniques in laser diodes and discusses different methods to measure laser facet temperature.

In chapter 2, the concept of thermoreflectance is explained. Measurement setup and image processing methods are presented.

Chapter 3 presents broad-area (100 µm) and narrow waveguide (7 µm) laser diode characterization: device performance, facet temperature, and COMD results.

Chapter 4 describes the concept of the multi-section laser diode method, motivation of this work and compares characterization results with standard laser diode results.

Chapter 5 introduces the implementation of the two-section method in LDs with different waveguide widths and array lasers. It presents the process steps and characterization results of the fabricated devices.

Chapter 2

Facet temperature measurement

2.1 Thermoreflectance (TR)

Thermoreflectance (TR) is a well-established non-contact surface temperature measurement method [22, 33, 34, 44, 45] having high temperature resolution [46, 47, 23, 48, 49]. It is based on the dependence of the relative change in reflectivity due to temperature change Figure 2.1, and given as:

$$\frac{\Delta R}{R} = (\frac{1}{R}\frac{\delta R}{\delta T})\Delta T = K\Delta T \tag{2.1}$$

where R is the reflection coefficient, ΔR is its relative change, ΔT is a temperature change, and K is the TR coefficient, which depends on the material and optical parameters of the TR setup, such as illumination wavelength, and NA of the objective [22].

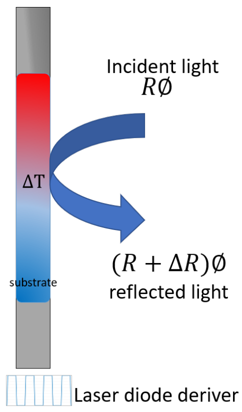

Figure 2.1: Schematic showing that TR measurement is based on the principle of variation of reflection with temperature.

2.2 Measurement setup

Figure 2.2 illustrates the schematic of the TR system utilized to measure the facet temperature of a LD.

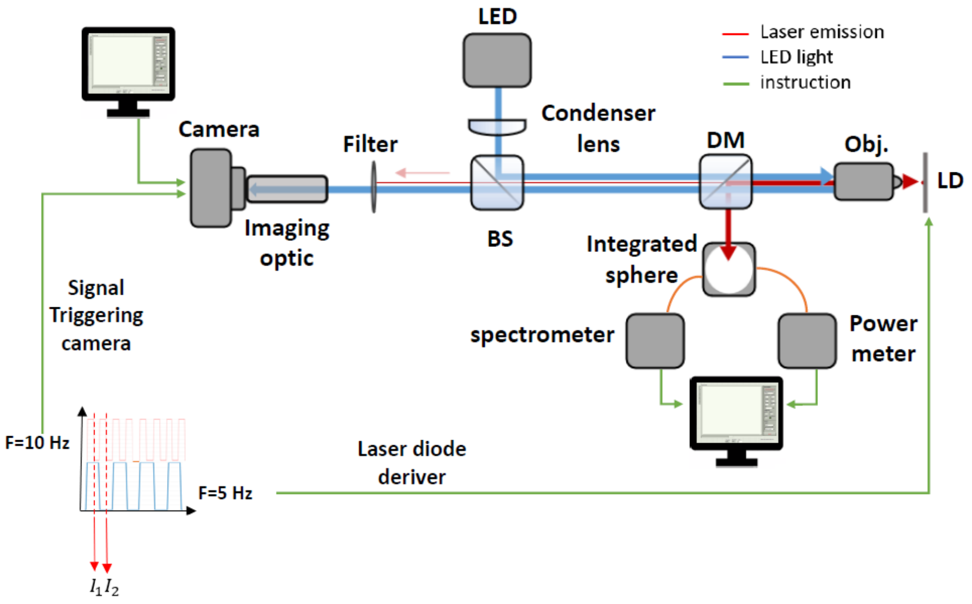

Figure 2.2: Schematic of the thermoreflectance setup.

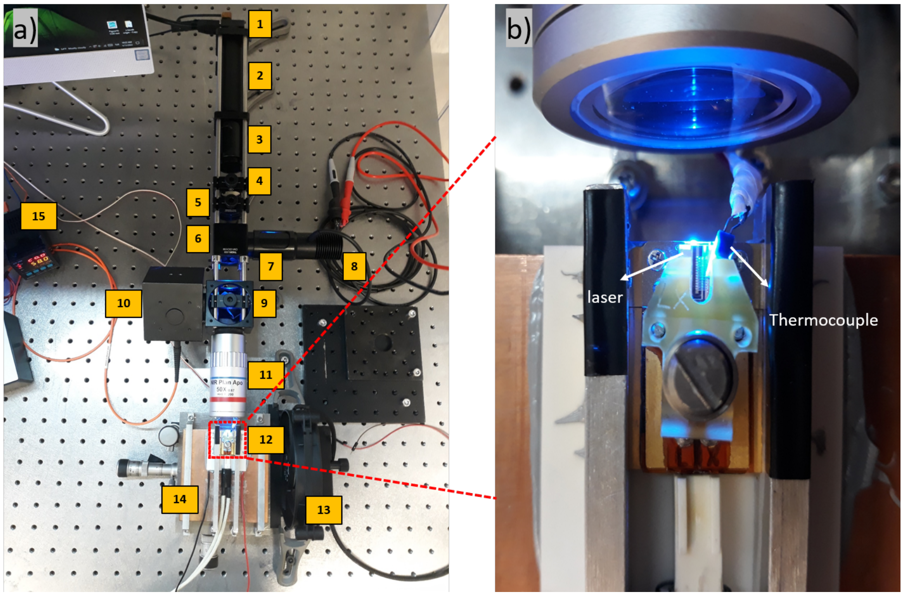

Figure 2.3: (a) Thermoreflectance setup and (b) LD on a heatsink

Figure 2.3 shows an LED at $\lambda = 470$ nm (8) passing through a condenser lens (7) to create a Kohler illumination setup for uniform illumination of the LD output facet (12). The LED light transfers through a beam splitter (BS) (6), a dichroic mirror (DM) (9), and a 50x (0.6 NA) NIR objective (11). The DM is chosen to reflect (99%) the LD emission and transmit the LED light. The LED light reflected from the LD facet is collimated by the objective and focused onto a camera (1) sensor by imaging optics (f=200 mm lens) (2) that provides a field-of-view larger than the emission area of the LD. Before the imaging optics, an additional filter (OD 6) (4, 5) is placed with a band-pass around the LED wavelength to eliminate any residual LD emission. Exploiting our setup, we were able to achieve a spatial resolution of 0.5 μm and a temperature resolution of 0.5 K. The reflected beam from the DM is coupled into an integrating sphere (10) to track LD power and wavelength, where they are used to measure the internal temperature (i.e., laser/junction temperature) of the LD . The LD is mounted on a carrier with a TEC underneath to control the heatsink temperature, and a fan (13) is used to cool down the heatsink (14). The temperature is measured by a thermocouple close to the LD, as shown in figure 2.3 (b).

During the TR measurements, the LD is driven by a square wave current at a frequency of 5 Hz (i.e., 100 ms pulse width with 50% d.c.). It is confirmed that such long pulses lead to a facet heating profile equivalent to continuous wave (CW) pumping. The camera is triggered by 10 Hz square waves to collect images at the falling edge of the signal. For every cycle of the current pulse, one image is obtained when the laser is ON and one when the laser is OFF. The basic working principle of the TR measurement is illustrated in the figure 2.4.

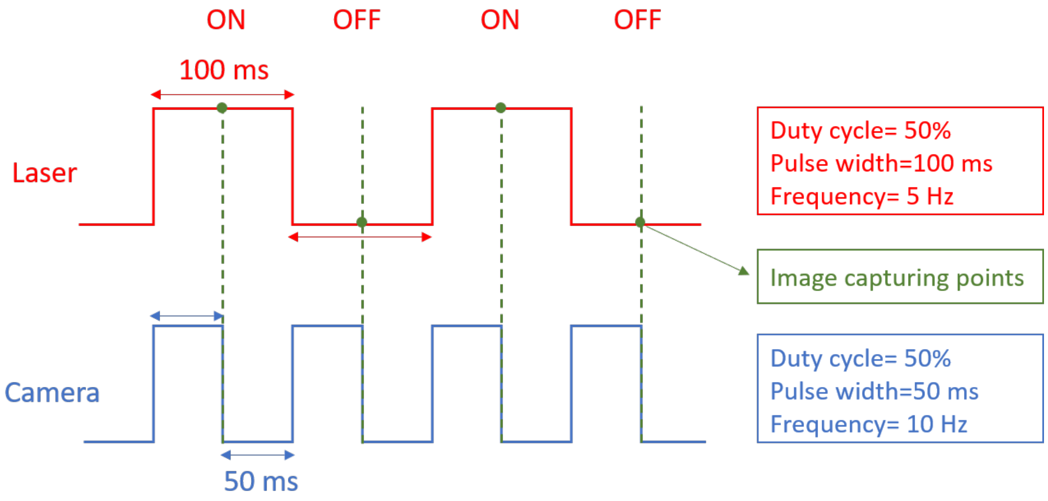

Figure 2.4: Working principle schematic of LD and camera for TR measurement.

1600 ON and OFF images were collected to increase the signal-to-noise ratio and obtain a high-quality thermal mapping of the LD facet. Image processing through Matlab was implemented to get the thermal images of the LDs facet.

2.3 Image processing

Figure 2.5 depicts the computer interface used to collect on and off images. The image in the figure is the near-field image of the LD and the bright area shows the LD output emission. ”Hot time” is the time position camera takes ON images, and ”Cold time” is the time position taking OFF images. ”N-image” is the number of images taken then doing averaging on them, and ”N-rep” is the number of doing this action. ”FPS (Hz)” is the camera trigger frequency, and ”exposure time” is the duration for the camera to collect light.

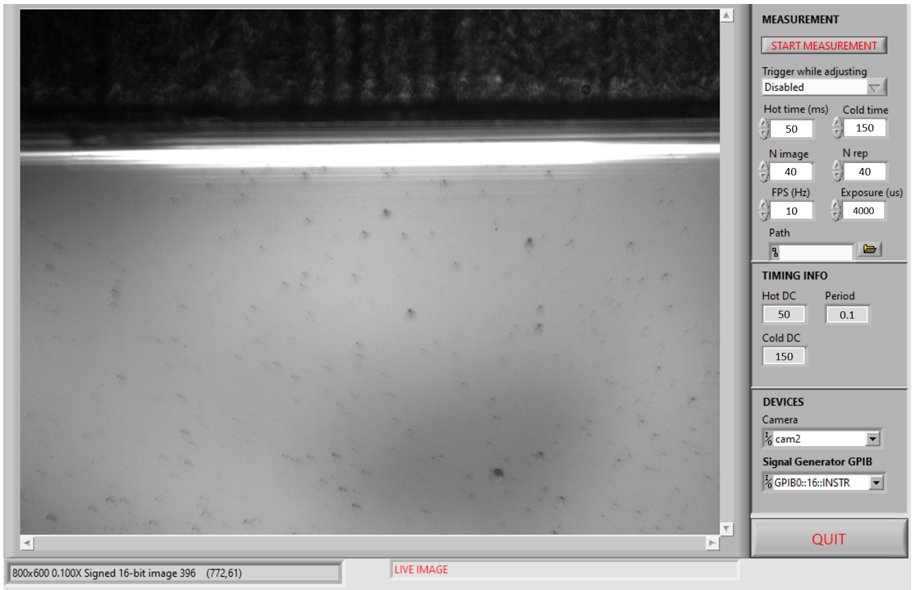

Trigger while adjusting
Disabled
Hot time (ms) 50
Cold time 150
N image 40
N rep 40
FPS (Hz) 10
Exposure (us) 4000
Path
Hot DC 50
Period 0.1
Cold DC 150
Camera
cam2
Signal Generator GPIB
GPIB0::16::INSTR
800x600 0.100X Signed 16-bit image 396 (772,61)

Figure 2.5: Computer interface for the measurement control.

First, the TR setup must be calibrated to acquire the TR coefficient (Kappa, K) as in equation (2.1). Two different techniques are utilized to find ’K’ for the GaAs substrate and AlGaAs active region. For the substrate, it is measured by varying the heatsink temperature with small steps over an extensive temperature range. For a known ΔT, the $\frac{\Delta R}{R}$ is recorded and K is calculated to be (2.2±0.1)$\times 10^{-4}$ K^{-1} as illustrated in figure 2.6.

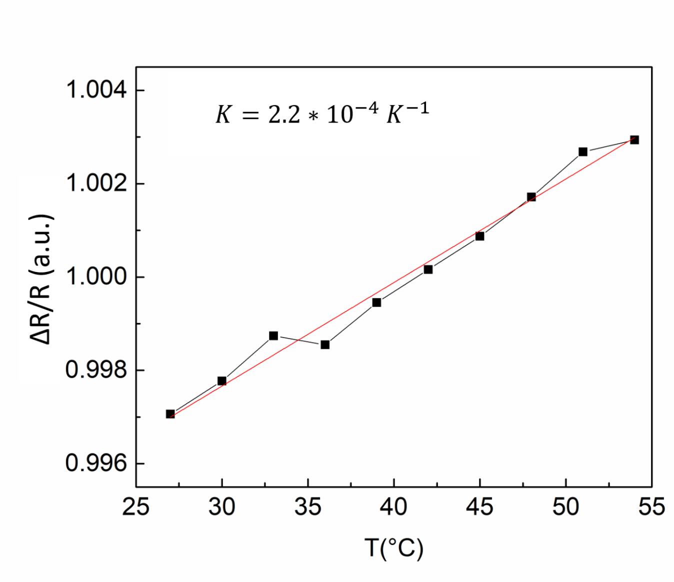

Figure 2.6: TR coefficient for the GaAs substrate

Another approach is used for the active region since its thickness is not enough to use the previous averaging method to find 'K'. First, the average junction temperature rise is measured for the LD by measuring the red-shift in the emission spectrum at sub-threshold currents, where we can safely consider that there is no optical absorption at the LD output facet [22], and the temperature on the facet is equivalent to the junction temperature. now that we know the temperature rise on the facet, the K value for the active region area can be obtained from equation 2.1 by calibrating the TR signal ($\frac{\Delta R}{R}$) which resulted in TR coefficient (K) as $(1.8 \pm 0.1) \times 10^{-4}\ K^{-1}$.

Figure 2.7 illustrates how the thermal map of the LD is measured utilizing images taken at on and off time of the laser diode, as explained before. The $\frac{\Delta R}{R}$ is calculated for every pixel of the I_1 and I_2 images shown in the figure 2.7 since they provide the facet reflectivity change:

$$\frac{\Delta R}{R} = \frac{I_1 - I_2}{\frac{I_1 + I_2}{2}} \tag{2.2}$$

where I_1 is the mean of the images taken at ON time and I_2 is the mean of the images taken at OFF time of the LD. These images are averaged over a large enough number of cycles (i.e., 1600 times in our measurements) to cancel the camera noise effects and obtain a high-quality image of the reflectivity change.

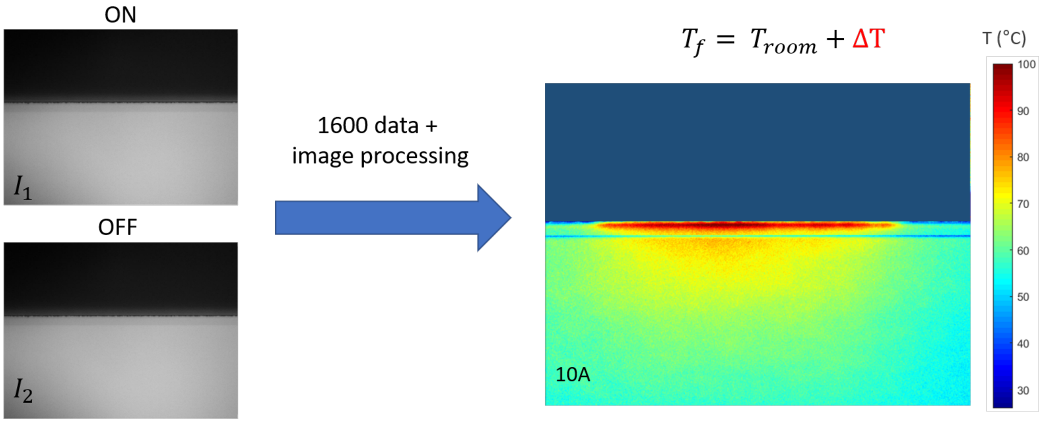

Figure 2.7: Obtaining LD facet temperature from raw data by doing image processing.

Going from the left side in the figure 2.7 (raw data) to the right side (temperature map), we need to apply two image processing steps. First, the flat field correction process is implemented to eliminate the background noise while taking the images. To do so, we need to take two other images named dark and flat images. The dark image is an image we take in the absence of any light. This means the LD, LED and room lights are off. The flat image is an image where light intensity is precisely the same in all pixels. We need to measure the flat field while the laser is off and the LED is on. These four images should all be recorded in the same session. Because dark and flat images depend on all the acquisition parameters and the temperature of the room. Second, we need to fix the possible shifts in the ON and OFF images due to thermal expansion. The thermal expansion causes the hot and cold images to be shifted with respect to each other. When we subtract those shifted images, we see artifacts needed to be corrected. So we measure the shift between the hot and cold images, and fix it by shifting the images in the opposite direction. In the end, by measuring $\frac{\Delta R}{R}$ and having K, we obtain the ΔT value. Adding room temperature, we get the temperature map of the LD output facet as shown in the figure 2.7.

2.3.1 Setup details:

The schematic design and components of the thermoreflectance assembly are shown in Figure 2.2 and 2.3 :

1) Camera: 2 MP resolution 60 FPS and 12 Bit CMOS based camera is used to view the laser facet illuminated by LED.

2) Tube: This tube with a diameter of 1 inch is mounted on the camera and prevents an external light source from coming into the camera, allowing a clear image to be obtained.

3) Achromatic doublet lens: It reduces the chromatic and spherical aberrations in facet imaging.

4) Short pass filter (λ<550 nm): This filter absorbs the laser light and passes the thermoreflectance signal (the reflected LED light from the laser facet).

5) Band pass filter (OD3): this filter is transparent for the LED light and absorbs Laser light. 6) Beam Splitter (BS): It reflects the LED light to illuminate the laser facet and transmits the thermoreflectance signal to reach the camera.

7) Plano-convex lens: It is a lens that works in the range of 350-700 nm with a 20 mm focal length with sanded surfaces (grit) to ensure alignment and uniformly spreading of the LED light.

8) LED: It is a 650 mW blue light source with a wavelength of 470 nm for illuminating the laser facet.

9) dichroic mirror (DM): this mirror is transparent for λ=400-630 nm (LED emission) and reflects λ=690-1600 nm (LD emission), it ensures that the LED light is transmitted and that a large (99%) part of the laser's emission is reflected into the integrating sphere.

Chapter 3

Standard LD characterization

In this chapter, I present the characterization results for broad-ara and narrow waveguide LDs.

3.1 Broad-area LD (100 µm wide)

3.1.1 Performance

Figure 3.1(a) shows the structure of the standard LD studied in this work. Figure 3.1(b) shows the LIV characteristic of LD with a 100 µm wide waveguide.

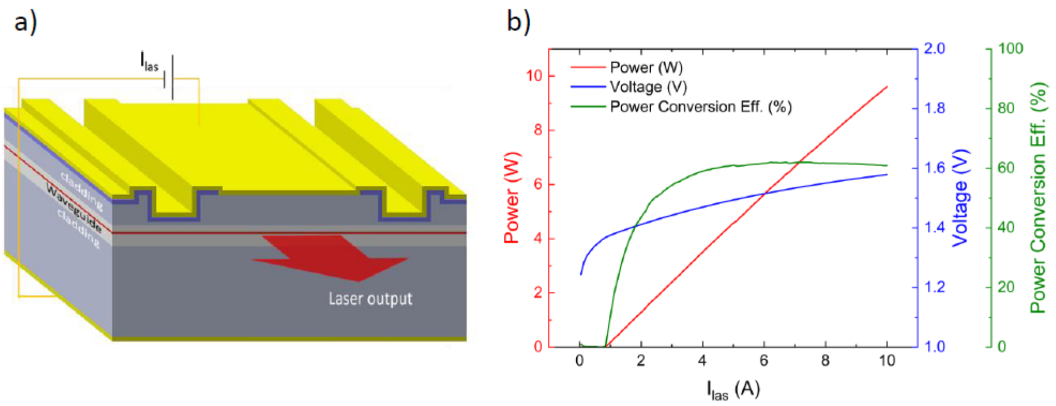

Figure 3.1: (a) Standard LD structure (b) LIV curve of standard LD under test.

3.1.2 Internal temperature

By exploiting the TR setup figure 2.2, the internal temperature (also called laser or junction temperature) of the LD can be measured simultaneously with the facet temperature. A correlation between these two temperature values is provided by tracking LD power and wavelength.

The desired laser internal temperature data can be obtained by multiplying the amount of power consumed by the laser with a constant known as thermal resistance, R$_{th}$:

$$T_{las} = R_{th} \cdot P_{waste} + T_{hs} \tag{3.1}$$

and P_{waste} is:

$$P_{waste} = I \cdot V - P_{op} \tag{3.2}$$

where I and V are the injecting current and voltage, respectively, and P_{op} is the optical output power of the LD. These values are extracted from LIV data in figure 3.1.

In order to calculate R$_{th}$, some characterization data of the LD is needed. First, we need to calculate the red-shift in the spectrum due to a change in temperature ($\Delta\lambda/\Delta T$). Next, we should calculate red-shift in the spectrum due to power lost in LD (P_{waste}) giving us ($\Delta\lambda/\Delta P_{waste}$). Then, R_{th} can be calculated as:

$$R_{th} = \frac{\frac{\Delta\lambda}{\Delta P_{waste}}}{\frac{\Delta\lambda}{\Delta T}} \tag{3.3}$$

To find ($\Delta\lambda/\Delta T$) value one needs the exact variation in temperature. Therefore, a change in laser temperature needs to be introduced externally by a temperature controller in the setup, while the contribution of laser heat load must be minimized. Hence, LD is biased by a pulsed current with a pulse width (PW) of 500 ns and duty cycle (d.c.) of 2 %. λ is measured at different temperatures ranging from 25 ℃ to 55 ℃ via an optical spectrometer (figure 3.2 shows an example of the spectral distribution result of the LD obtained using the Ocean Optic spectrometer). Then, $\Delta\lambda/\Delta T$ of 0.3 nm/℃ is calculated from the slope in figure 3.3 and 3.4 where the wavelength is plotted versus temperature.

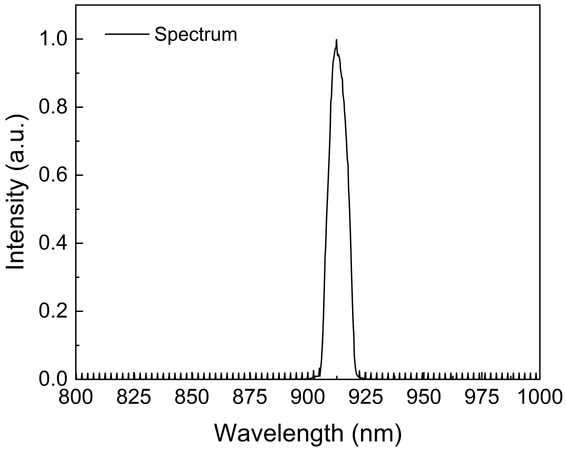

Figure 3.2: Sample spectrum graph obtained with a spectrometer.

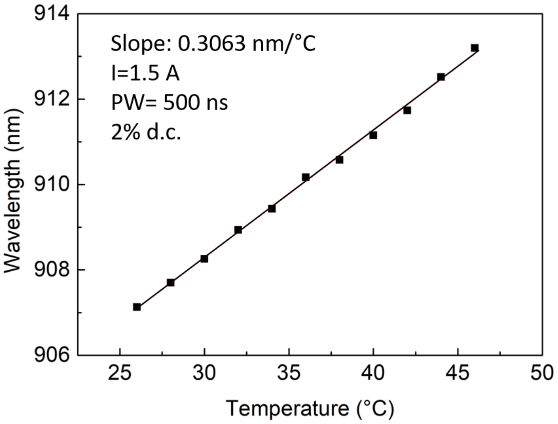

Figure 3.3: Wavelength variation with temperature at 1.5 A.

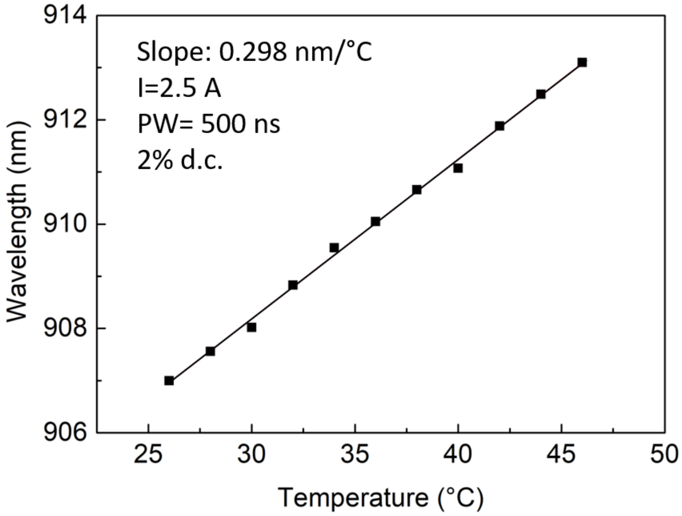

Figure 3.4: Wavelength variation with temperature at 2.5 A.

To find $(\Delta\lambda/\Delta P_{waste})$ value, we measured the LD spectrum at a fixed temperature (25 ℃) while injecting various currents in CW mode. Then, we plot wavelength as a function of P_{waste} where the slope of the graph will be $\Delta\lambda/\Delta P_{waste}$ value. P_{waste} at each current is calculated by using equation 3.2.

Then, we plot wavelength as a function of P_{waste} giving $\Delta\lambda/\Delta W$ as 2.349 nm/W. Using both $(\Delta\lambda/\Delta T)$ and $(\Delta\lambda/\Delta W)$ for the desired LD, the R_{th} is calculated by equation 3.3 as 7.83 ℃/W, and the internal LD temperature (T_{las}) at all currents can be calculated using equation 3.1. Figure 3.5 (b) shows T_{las} of the LD .

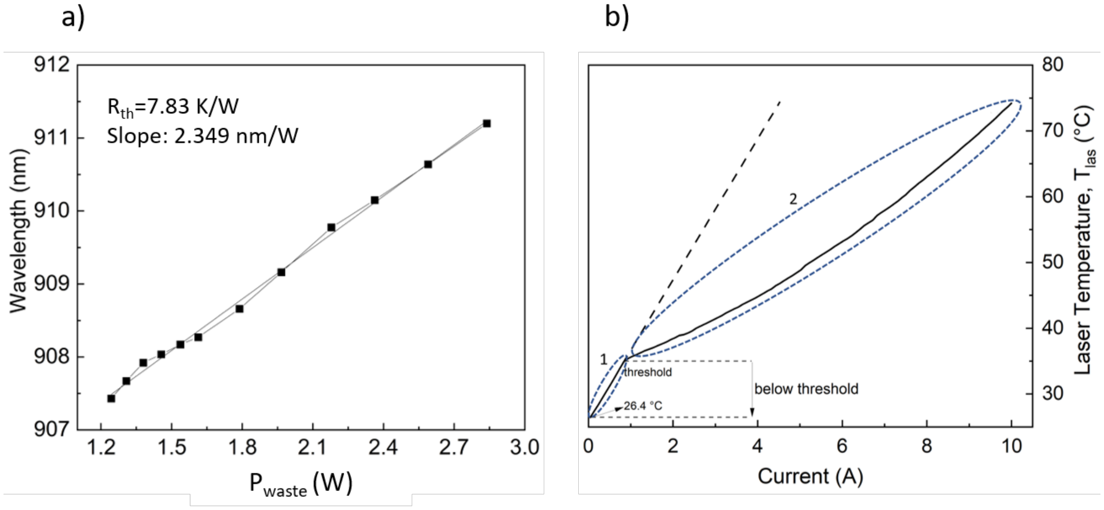

Figure 3.5: (a) Wavelength vs P_{waste} (b) Standard LD internal temperature.

Figure 3.5 (b) presents standard LD internal temperature (T_{las}). There are two regions, one below and one above the threshold. Below threshold current, LD temperature increases linearly due to not having output power, so the equation 3.2 will reduce to:

$$P_{waste} = I \cdot V \tag{3.4}$$

It indicates a linear increment in temperature, whereas it has exponential behavior for the above threshold region. If there were no output power, T_{las} would increase linearly in the above I_{th} region, as depicted with the dashed line in the figure.

3.1.3 Facet temperature

Facet temperature of a LD can be simplified as:

$$T_{fac} = T_{las} + T_{abs} \tag{3.5}$$

Where T_{las} is the laser internal temperature and T_{abs} is the change in facet temperature due to absorbed laser output power by the facet.
Figure 3.6 presents the 2D temperature characterization results of the standard LD (i.e., L_{win}=0 µm, I_{win}=0). The schematic of the standard LD is shown in figure 3.6 (a), and the enlarged view corresponds to the surface temperature map of the LD waveguide at I_{las}=10 A. The hottest spot represents the QW temperature and center of the lateral waveguide. Figure 3.6(b) displays the facet temperature (T_{fac}) maps for I_{las} from 2 to 10 A. The heat spreads from the active region down toward the heatsink. The slight asymmetry of the temperature maps between the right and left sides is due to the test setup's cooling configuration, which helps us maintain LD temperature at a fixed temperature throughout the measurement. The sequence clearly shows that T_{fac} increases with higher injected current.

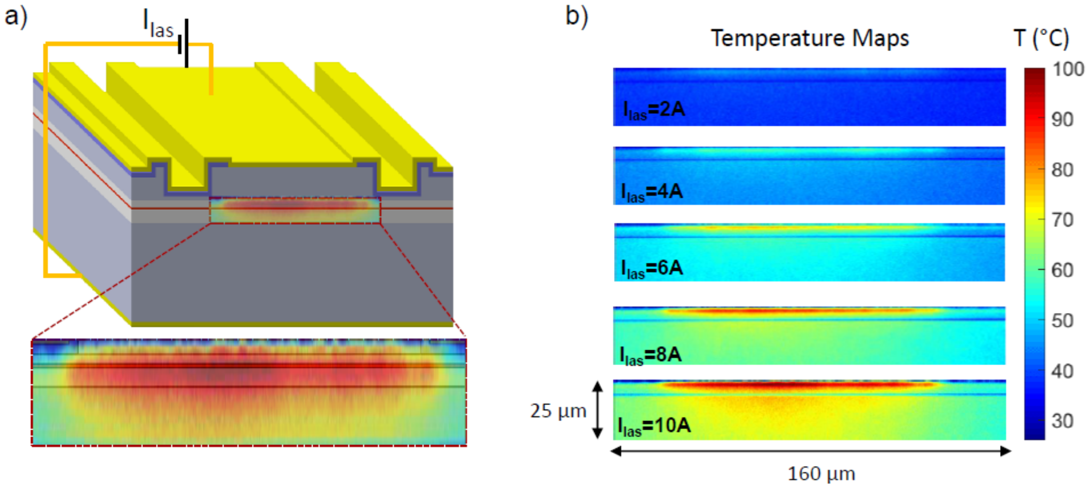

Figure 3.6: (a) Standard LD structure and enlarged image corresponds to the hottest facet for I=10 A. (b) Facet temperature distribution map at currents ranging from 2 to 10 A.

Figure 3.7 shows the 2D zoomed view of the enlarged image in Figure 3.6(a), depicting the detailed temperature map of the LD facet. The peak facet temperature, $T_{fac,peak}$, is around 105 ℃, and it is much higher than the T_{las}= 75 ℃. As mentioned before, the critical temperature (T_c) for COMD occurrence is around 120 - 150 ℃. Therefore, it is likely that this LD is operating close to the COMD point.

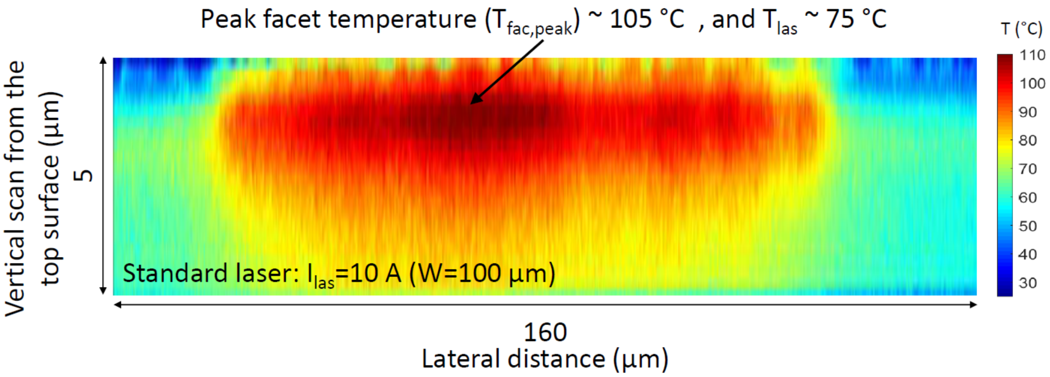

Figure 3.7: An enlarged view of the facet temperature map at I_{las}=10 A.

Figure 3.8 (a) presents the output power (P_{out}) and laser temperature (T_{las}) versus I_{las}. Figure 3.8 (b) presents the vertical profile of the facet temperatures as a function of the distance from the top of the LD to the GaAs substrate (solid lines) and the T_{las} (dashed lines) for I_{las} from 2 to 10 A. For T_{fac}, temperature values are averaged along the 40 µm width of the waveguide center. It can be seen that the difference between T_{fac} peak and T_{las} increases with I_{las}, possibly due to an exponential increment in waveguide temperature as indicated in figure 3.8(a), and also the increased optical absorption of the LD light by the facet at higher output powers.

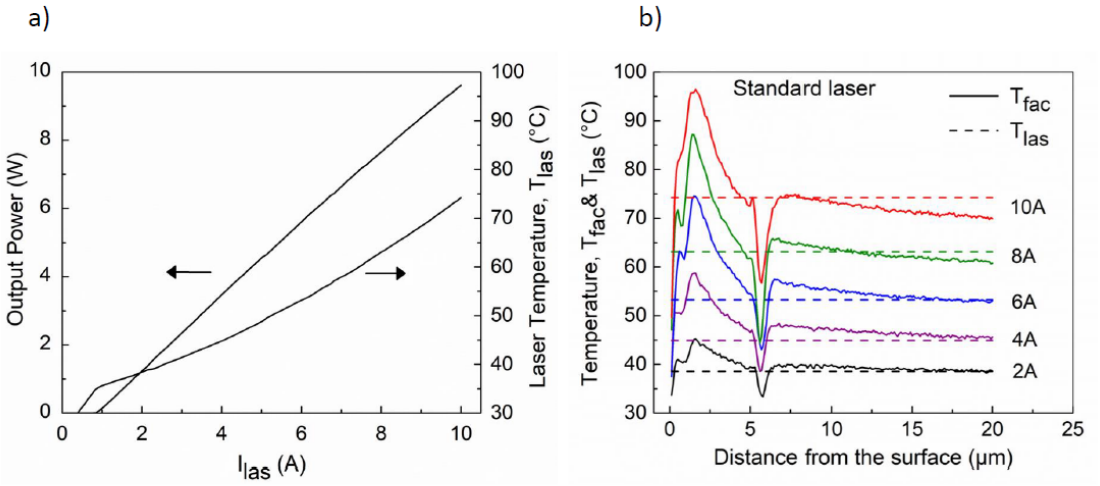

Figure 3.8: (a) Variation of laser output power and laser temperature with current. (b) Variation of laser and facet temperatures at different currents.

3.1.4 COMD test

After investigating LD's internal and output facet temperature, we tested LDs under high currents to explore the COMD failure of the device. Figure 3.9 (a) shows a typical L-I curve up to I_{las}=20 A under CW operation. The TEC temperature was kept at 20°C for testing to reduce the thermal effects caused by the p-up assembly. There is a sudden drop in output power, as seen from the graph, where the maximum power and corresponding current are 13.1 W and 14.5 A, respectively. An optical microscope image shows a COMD spot in the epitaxial layer as depicted in enlarged figure 3.9 (b). Investigating further, we checked the top view of the laser cavity by electroluminescence (EL). Figure 3.9 (c) shows that dark line defects (DLDs) extend approximately $\frac{2}{3}$ from the "COMD point" into the active region.

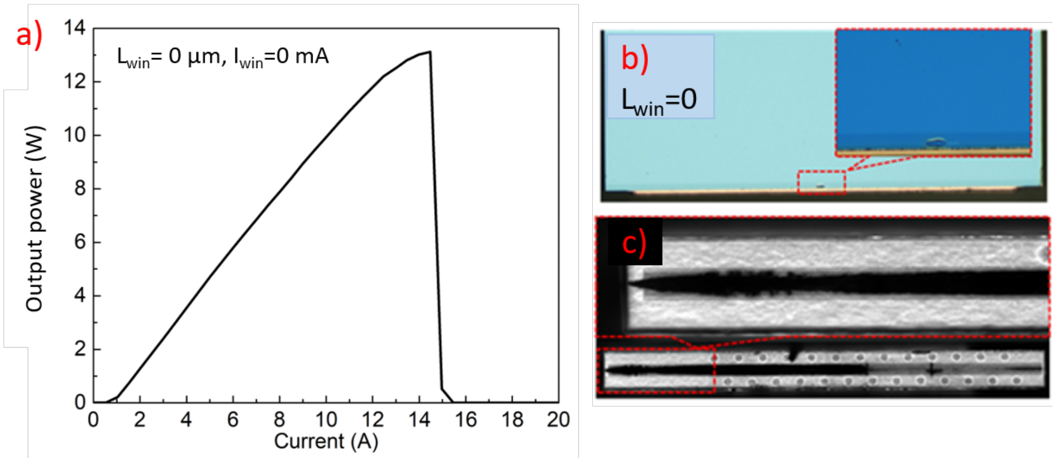

Figure 3.9: LD failure test. (a) output power versus current for LD with L_{win}=0, under CW, 20 ℃ operation. (b) optical microscope image of the LD output facet. (c) EL image of the laser cavity.

3.2 Narrow waveguide LD (7 µm wide)

Single mode LDs have narrow waveguides of 5 µm, and they are key components in optical fiber communication at λ= 975 nm. In this section, we studied LDs with near single-mode characteristics. After analyzing the standard broad-area 100 µm wide LD, we investigated the junction and output facet temperature of a 7 µm wide LD to see how the waveguide width would affect both junction and facet temperature.

3.2.1 Performance

Figure 3.10 (a) shows the schematic structure of the LD where the emission width is 7 µm, and 3.10(b) shows the LIV characteristic of the device. The highest efficiency is 61.4 % at 1A current. The instability in the efficiency curve that accrues around 1.74A is due to having higher order mode emission.

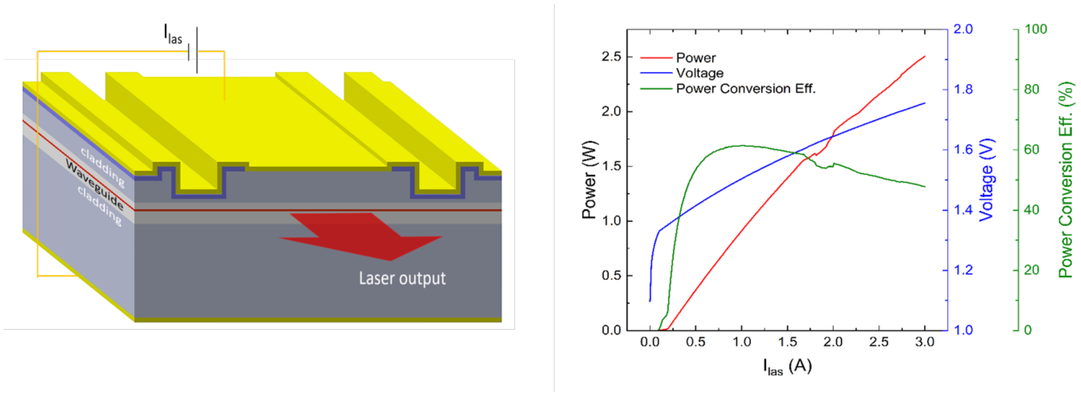

Figure 3.10: (a) 7 µm width laser diode structure (b) LI curve of the LD under test.

3.2.2 Internal temperature

As described in section 3.1.2, we can measure LD internal temperature using equations 3.1, 3.2, 3.3, and knowing laser LIV data. As mentioned in the previous section, first we need to find R_{th}, and based on equation 3.3 we need $\Delta\lambda/\Delta P_{waste}$ and $\Delta\lambda/\Delta T$ values. To find $\Delta\lambda/\Delta T$ value, we did measurement as described in 3.1.2 and slope of the curve in the figure 3.11 results in 0.369 nm/°C. Next we found $\Delta\lambda/\Delta P_{waste}$ value. We implemented measurement as described in 3.1.2 and obtained a value of 2.8 nm/W. Calculated R_{th} value for this LD based on equation 3.3 is equal to 7.6 °C/W and figure 3.12 (b) depicts the resulting internal temperature of the LD.

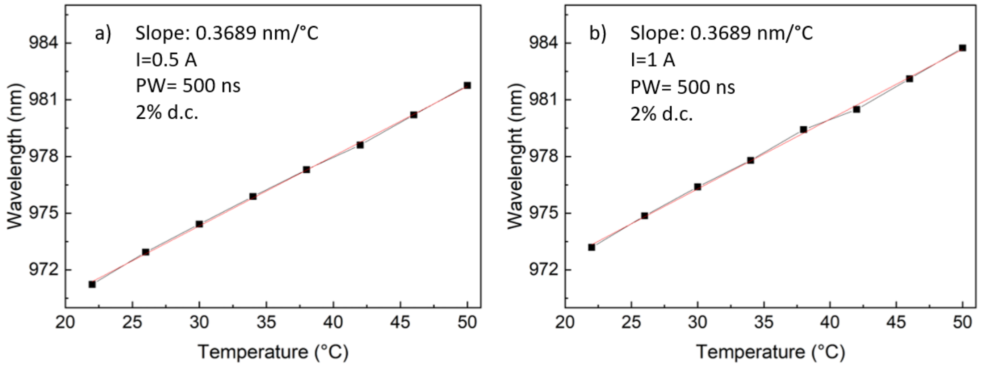

Figure 3.11: Wavelength variation with temperature (a) at 0.5 A (b) at 1A.

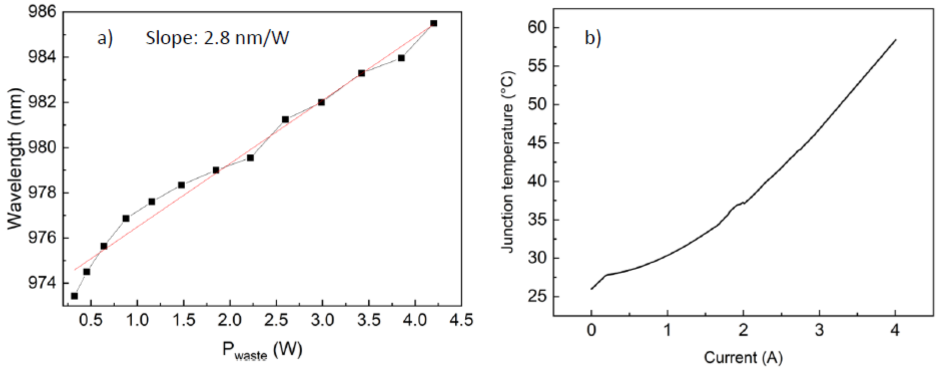

Figure 3.12: (a) Wavelength variation with waste power at fixed temperature = 25 °C. (b) Junction temperature (T_{las}) vs. current.

3.2.3 Facet temperature

Figure 3.13 (a) displays the facet temperature (T_{fac}) maps for I_{las} from 1 to 4 A. The heat spreads from the active region down toward the heatsink. As it can be seen from the figures, the heat is restricted to the waveguide width (7 µm), and the hottest spot is around the epitaxial layers. Figure 3.13 (b) is a vertical scan of facet temperatures showing T_{fac} as a function of the distance from the top of the LD to the GaAs substrate (solid lines) and the T_{las} (dashed lines) for I_{las} from 1 to 4 A. For T_{fac}, temperature values are averaged along the 7 µm waveguide width. It can be observed that the difference between T_{fac} peak and substrate temperature increases with I_{las}, possibly due to exponential increment in waveguide temperature as indicated in figure 3.12 (b), and also the increased optical absorption of the laser by the facet at higher output powers.

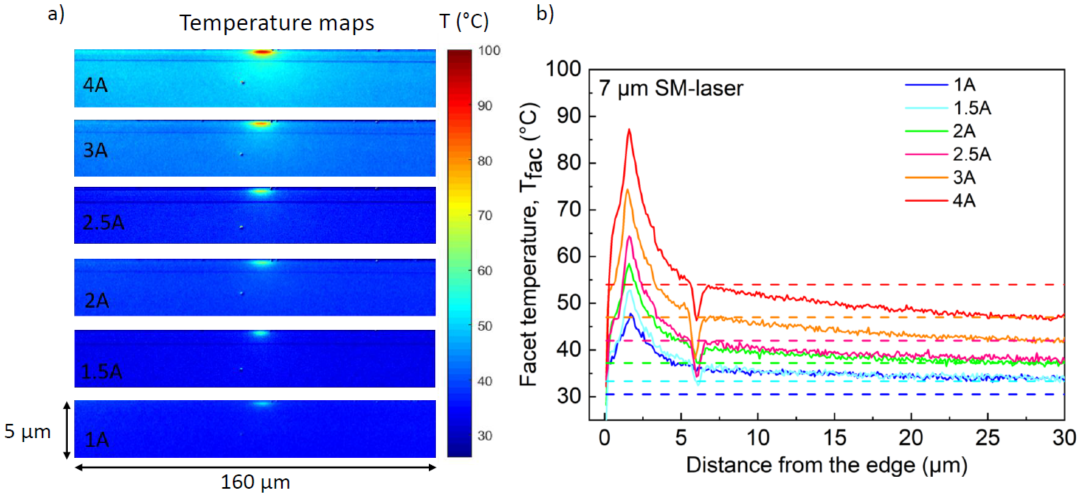

Figure 3.13: (a) Output facet temperature maps of the LD with 7 µm waveguide width (b) LD internal and facet temperature at different currents.

The current density in this LD is much higher than 100 µm wide broad-area LD. For example, to have the same current density as the 100 µm broad area laser at 10A, the 7 µm narrow waveguide need to be biased to 0.7 A current. Therefore, by comparing figure 3.6 (b) with figure 3.13 (a), it can be concluded that narrow waveguide LDs have much higher current densities while their facet temperature is lower.

Figure 3.14 shows the facet temperature map of this LD at 4A.

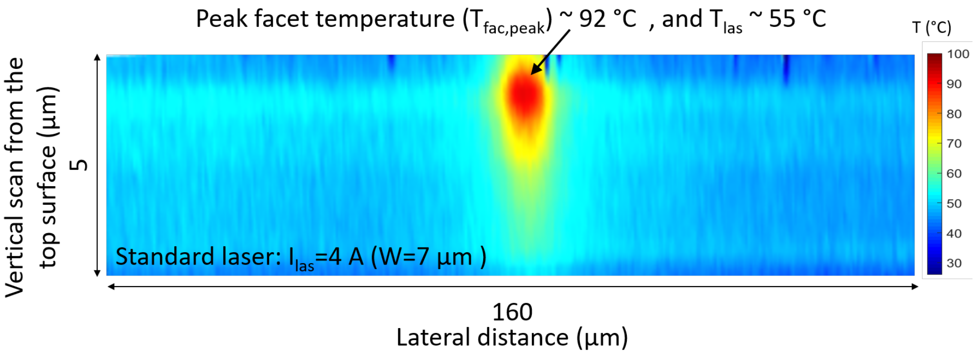

Figure 3.14: An enlarged view of the 2D waveguide temperature at $I_{lase} = 4$A.

Comparing figure 3.14 & 3.7 demonstrates that narrower waveguide have much lower internal and facet temperatures even at much higher injection current and output power densities. This indicated that narrower waveguide LDs should be more robust against COMD failure.

Chapter 4

Multi-section laser diode

As mentioned before, the self-heating of the LD raises its cavity temperature and additional heat generation mechanisms on the facet (e.g., non-radiative recombination, optical absorption by surface states) cause the facet temperature to be even higher than the cavity [31, 50]. However, the 2-section design restricts the thermal impact of the laser section on the facet. This approach led to facet temperatures lower than the laser cavity for the first time [35, 36].

Figure 4.1 schematically depicts the concept of heat separation by exploiting a 2-section structure. In standard LD shown in fig 4.1 (a), the junction temperature is approximately constant along the cavity, and it contributes directly to the facet temperature. On the other hand, in the two-section structure shown in (b), LDs' main heat load is separated from the output facet via an electrically pumped transparent window. In this work, by utilizing the multi-section waveguide method, we fabricated and carried out a detailed characterization of the devices, investigated their optimum working conditions (i.e., similar output power with much lower facet temperature compared to the standard LDs), and demonstrated elimination of COMD in LDs.

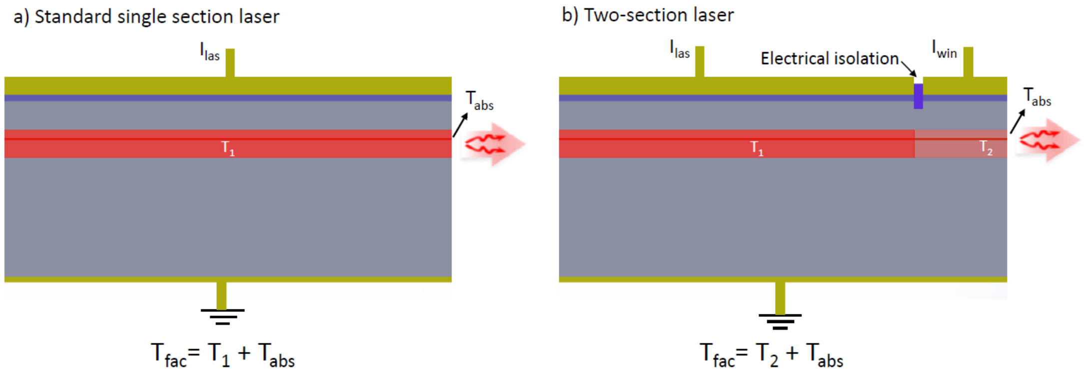

Figure 4.1: Schematic description of internal heat in (a) standard LD, and (b) two-section LD.

4.1 Device design

The semiconductor laser with a 2-section structure used in the project is shown in Figure 4.2. The laser and window regions are electrically isolated by an isolation channel. No current will pass to the other side under the voltage applied to these sections. However, the two regions are optically connected, and the isolation channel does not introduce optical loss. The highly doped layers in these regions are removed by a wet etching step in the fabrication process, where electrical communication between the two sections is cut off. After etching, this area is also covered with a dielectric insulator. In the end, the device consists of a laser section with length L_{las} and a window section with length L_{win}. These two regions can be driven by independently controllable laser (I_{las}) and window (I_{win}) currents. Fabricated GaAs-based 915 nm LDs have 100 µm wide waveguides with a total cavity length (laser and window sections) of 5.0 mm. Five designs with L_{win}=0, 250, 500,1000,1500 µm are fabricated to study the multi-section LDs systematically.

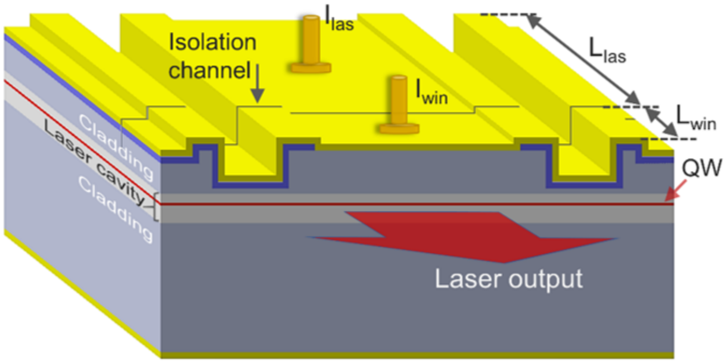

Figure 4.2: Schematic description of the multi-section LD.

The formation of an unpumped window near the facet region (20-50 µm) prevents the propagation of carriers towards the laser surface, thus reducing free carriers. In this way, the non-radiative recombination decreases, reducing the temperature formed on the surface. The unpumped window length is the same for both the standard and 2-section lasers.

4.2 Fabrication

In this work, we employed a high-efficiency GaAs-based epitaxial structure with a single quantum well (QW) active region [51, 52]. Figure 2 shows the process flow schematic of the multi-section laser. (a) A wet chemical etching process was applied to form a ridge waveguide structure with 10 µm wide and 0.8 µm deep trenches along the cavity. (b) Then, a 20 µm wide and 0.35 µm deep trench is formed perpendicular to the cavity to divide the waveguide into two sections along the cavity. (c) A dielectric film was deposited as an insulating layer. (d) A current injection region pattern was formed by selective etching of the dielectric film. (e) Ti/Pt/Au layers were evaporated as p-contact followed by lift-off between the two sections. (f) After wafer thinning, n-metal was deposited on the bottom of the wafer. The wafer was cleaved into bars, where high reflectivity (95%) and low reflectivity (1%) films were coated on the back and front facets, respectively. The bars were cleaved into single emitters and soldered on AlN heat sinks as p-side up.

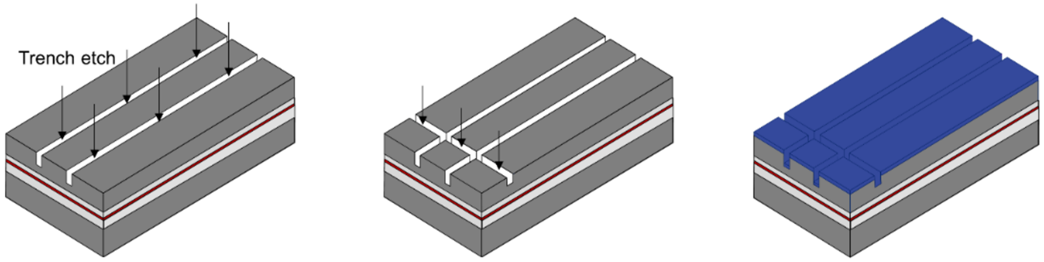

(a) Waveguide formation (b) Electrical isolation each (c) Dielectric film deposition

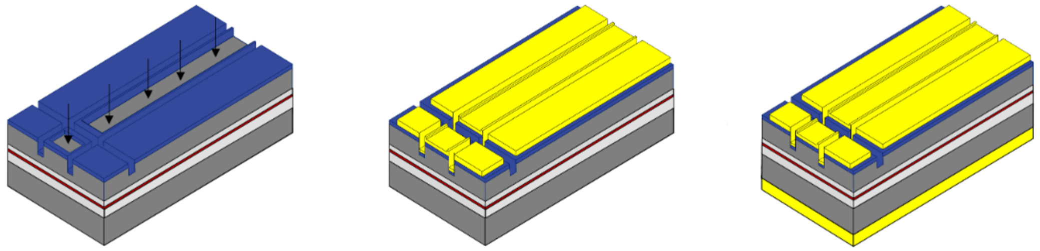

(d) Pump window opening (e) P-metal deposition (f) N-metal deposition

Figure 4.3: Schematic of the multi-section LD fabrication process.

The LDs have electrically isolated laser and window sections along the cavity, as described in Figure 4.2. Figure 4.4 shows the IV curve via which we can measure the resistance between laser and window sections in each of the LDs as it can be seen from the inside figure to be around 150 Ω, which shows electrical isolation of the laser and window regions.

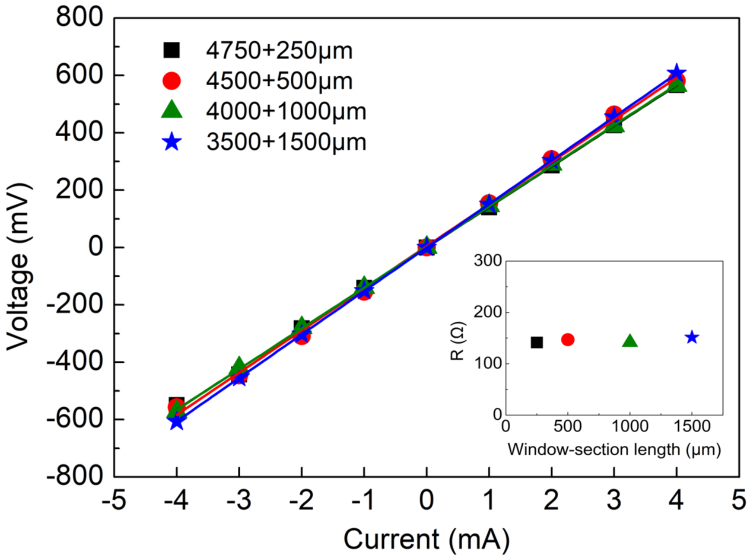

Figure 4.4: Resistance comparison of 4750+250µm, 4500+500µm, 4000+1000µm, 3500+1500µm LDs.

4.3 Characterization

In our setup figure 2.2, as mentioned before, we can measure the near-field profile for the facet temperature measurement, LD power, and spectrum simultaneously. As depicted in figure 4.5, a high-power laser diode driver (an ILX36000) is used to bias LDs, and the camera is triggered via an LXI signal generator, which is synchronized with the ILX driver to get laser facet images at the desired time. Also, a current source is used for LED illumination, which is our thermoreflectance signal. To measure LD's power and spectrum, we used a Thorlabs power-meter and an Oceanoptic spectrometer, respectively, as shown in figure 4.6.

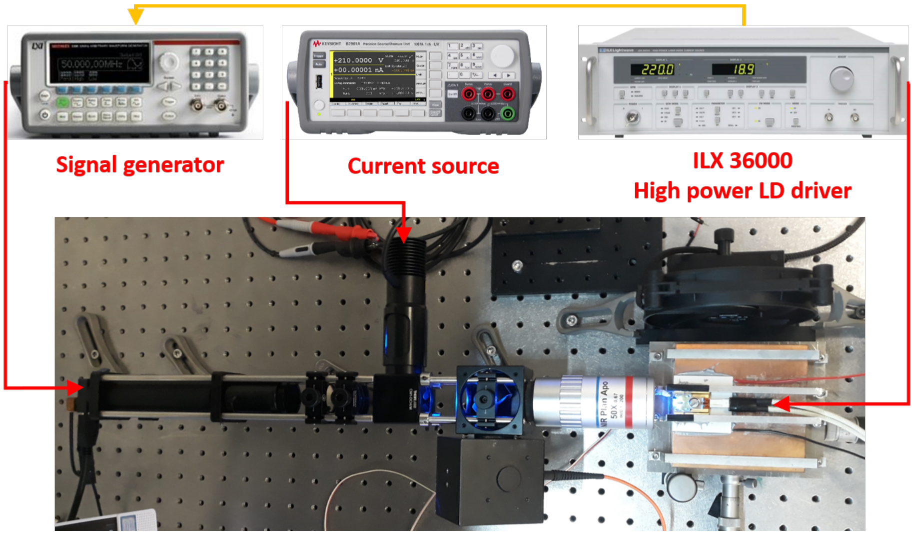

Figure 4.5: Thermal reflection setup and connections.

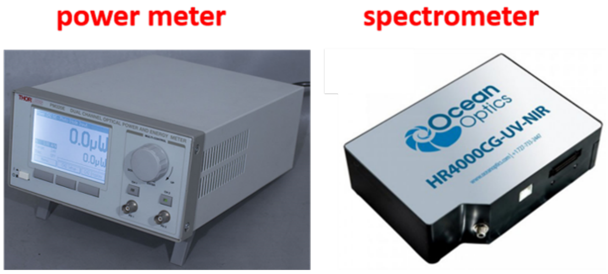

Figure 4.6: Power meter and spectrometer used in the study.

4.3.1 Performance

We explored five LD designs with L_{win}=0, 250, 500, 1000, 1500 µm for their electro-optical performance and temperature characteristics. First, LDs were characterized with I_{win}=0 mA and then investigated for their I_{win} dependent behavior. Finally, we focused on the best performing multi-section LDs with L_{win} of 500 and 1000 µm and implemented failure tests compared to the standard LD (L_{win}=0 µm).

The measured CW L-I data in Figure 4.7 (a) show that the output power reduces with longer L_{win}, even a rollover for L_{win}=1500 µm after 9 A. Figure 4.7(b) compares the slope efficiency and the threshold current (I_{th}) of the LDs. The slope decreases almost linearly with longer L_{win}, confirming that the longer unpumped window length will introduce more absorption losses. The I_{th} increases slowly for L_{win} from 0 to 500 µm, which is caused by the competition of lower I_{th} of shorter cavity length but higher loss due to unpumped window. When L_{win} increases further to 1000 and 1500 µm, I_{th} increases significantly, indicating that the loss increase influence is stronger compared to the shorter cavity length advantage. These are all measured without injecting I_{win}, and we know that the window region absorbs laser light under this circumstance.

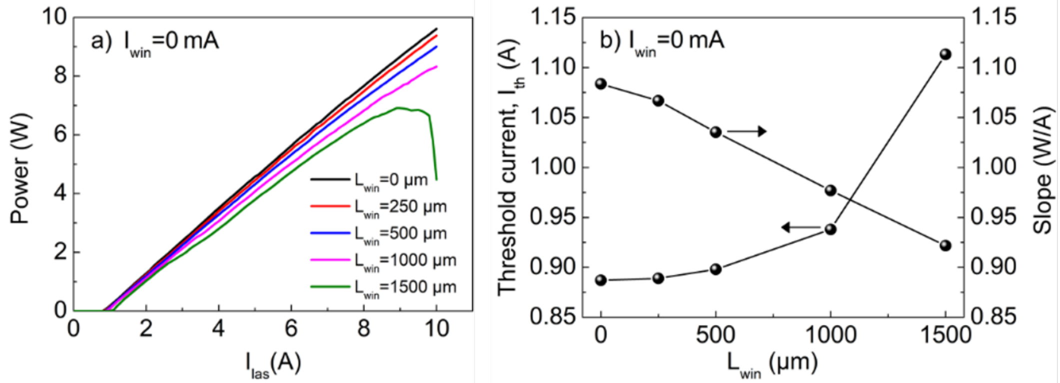

Figure 4.7: Experimental results under CW operation at 25 ℃. (a) power vs. current curves for different L_{win} structures. (b) threshold current and slope vs. L_{win}.

Next, we applied I_{win} and investigated how output power would change with respect to that. To do so, we should know the I_{win} limit for each design in order to make the window section transparent. The transparency current, I_{tra}, can be calculated for each of the two-section LDs using [53]:

$$J^d_{tra} = J^0_{th} - \alpha_i\left(\frac{tan\theta}{2ln(\frac{1}{R_fR_r})}\right) \tag{4.1}$$

Where J^d_{tra} is the transparency current density, J^0_{th} is the threshold current density at the infinite cavity length, α_i is the internal loss, tanθ is the slope of the graph, figure 4.8 (a), where we plot J_{th} versus inverse cavity length, R_f and R_r are the front and rear reflectivities. The J_{th} and tanθ are found to be 80 ± 5 A/cm^2 and 18.8 ± 1.2 A/cm. α_i is equal to 0.47 cm^{-1} [51] and R_f and R_r are 0.03 and 0.97, respectively. Transparency current density is calculated to be 78.98 A/cm^2.

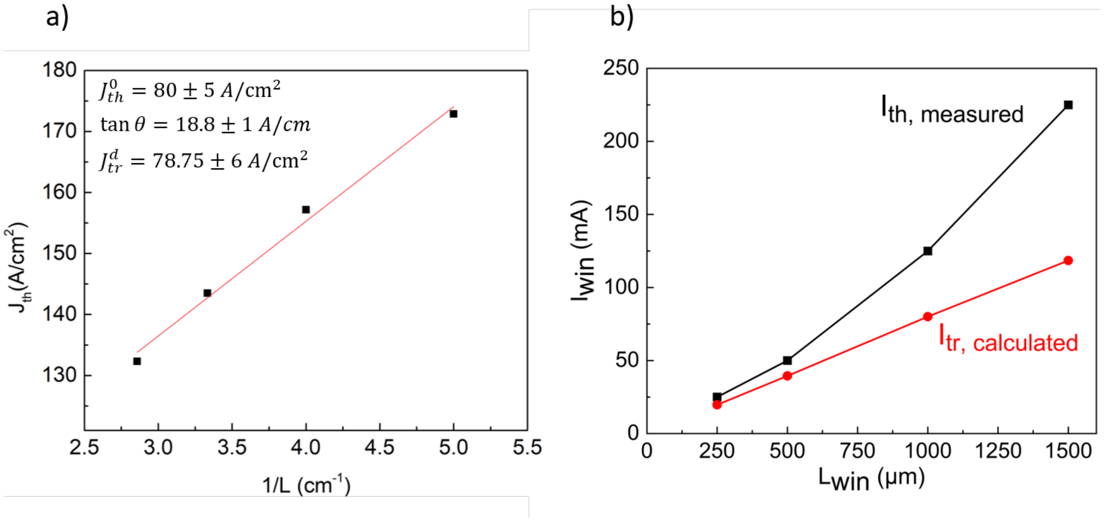

Figure 4.8: (a) The threshold current density as a function of inverse cavity length [28]. (b) Transparency and threshold current for each window length.

In figure 4.8 (a), the experimental results of threshold current density as a function of inverse cavity length are given for high power diode laser with 100 μm width.

Figure 4.8 (b) shows the threshold and transparency currents calculated from equation 4.1 for each two-section LD. Now we have the value of transparency current; we investigated how I_{win} affects output power. We injected I_{win} with 25 mA steps and measured the output power of the two-section LDs in comparison with the standard single section LD at I_{las}= 5A in CW mode. For each two-section LD, we increased the I_{win} limit to a level that its output power is higher than that of the standard LD, as shown in the figure 4.9. We showed that the output power of a 2-section LD is comparable with the standard LD, so there is no power degradation when LDs were pumped with a proper I_{win} current.

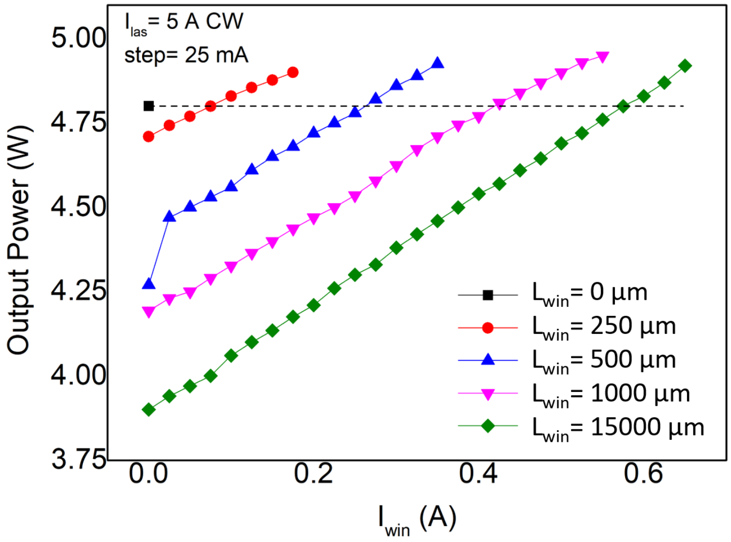

Figure 4.9: I_{win} effect on output power of two-section LDs.

Figure 4.10 (a) demonstrates the L-I-V and power conversion efficiency (PCE) characteristics of the L_{win}=500 µm LD with I_{win}=0, 200, 400 mA under CW operation at 25 ℃. The power increases with higher I_{win} due to a lower threshold and improved slope efficiency. The slope efficiency increase with higher I_{win} is due to lower absorption loss. The maximum PCE at I_{win}=400 mA is 64.6%, which is 6% and 3.3% larger than I_{win}=0 mA and I_{win}=200 mA, respectively. Similarly, Figure 4.10 (b) shows the L-I-V and PCE characteristics of the L_{win}=1000 µm design with I_{win}=0, 400, 800 mA under CW operation at 25 ℃. The power of the LD with I_{win}=800 mA is 9.2 W at 10 A, which is 1.3 W and 0.4 W larger than I_{win}=0 mA and I_{win}=400 mA, respectively. The L-I curve of LD with I_{win}=800 mA shows two different slopes switching around I_{las}=0.9 A, which the reason is not apparent yet and requires further study. In these tests, I_{win} is used to recover the absorption losses without generating heat. Hence, the I_{win} limit is set by comparing the facet temperatures that we will discuss in the next part.

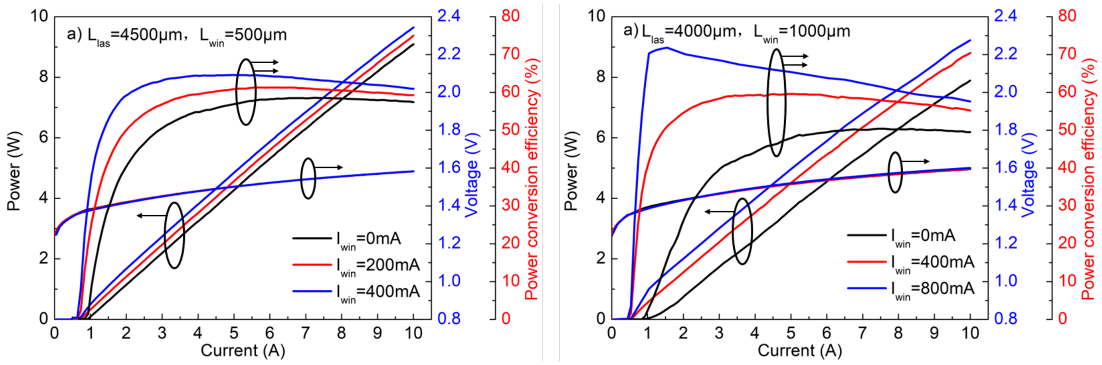

Figure 4.10: I_{win} effect on performance of two-section LDs. (a) L_{win}=500 µm and (b) L_{win}=1000 µm.

4.3.2 Internal temperature

As described in section 3.1.2, we can measure LDs internal temperature (i.e. laser temperature) using equations 3.1, 3.2, 3.3, and LIV data. As mentioned in the previous section, first we need to find R_{th}, and based on equation 3.3 we need $\Delta\lambda/\Delta P_{waste}$ and $\Delta\lambda/\Delta T$ values.

To find ($\Delta\lambda/\Delta T$) value, we did measurement as described in 3.1.2 and slope of the curve in the figure 4.11 gives the value to be 0.3 nm/°C. This value is the same for the standard single section laser diode due to having the same active region. Moreover, since the laser is biased to a short PW (500 ns) and d.c. (2 %) there is almost no heat generated inside the devices.

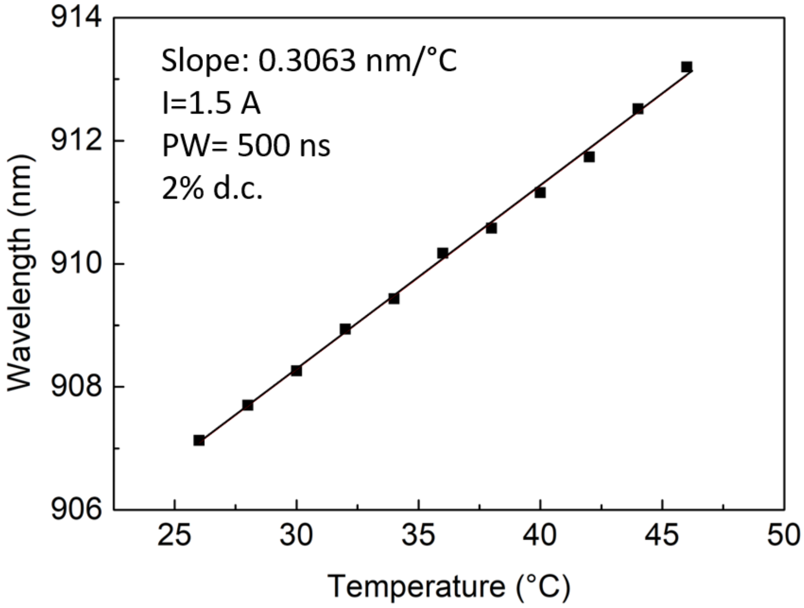

Figure 4.11: Graph of wavelength variation with temperature at 1.5 A.

Next, we characterized LD output power while injecting I_{win} at transparency level and above.

To find $\Delta\lambda/\Delta P_{waste}$ value, we did measurement as described in 3.1.2. Then we plot wavelength as a function of waste heat for each LD separately because the heating inside the cavity is now not the same for them due to different L_{win}, which is directly related to the output power.

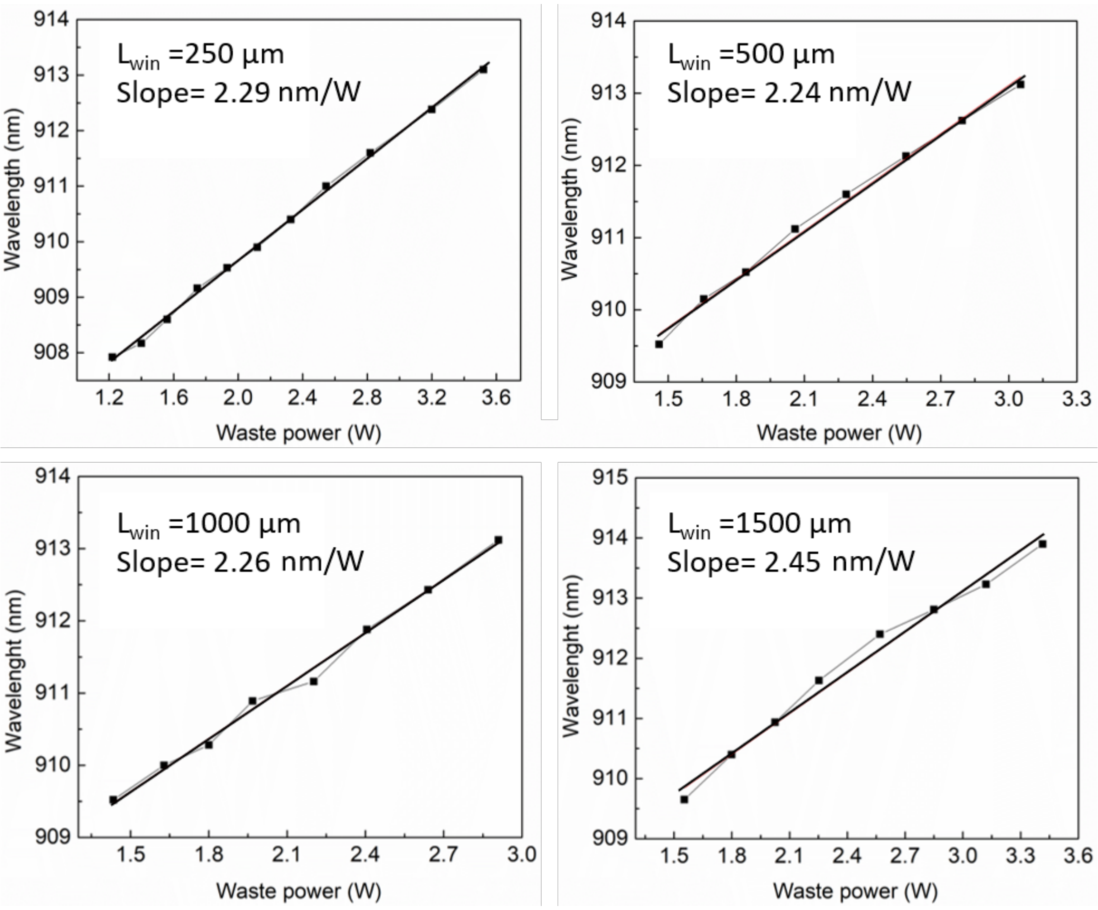

Figure 4.12: Graphs of wavelength variation with waste power at T= 25 °Cfor each LD with L_{win}.

Calculated R_{th} value for these LDs and single section LD is shown in the figure 4.13 (a). The thermal resistance (R_{th}) values are similar for 0 to 1000 µm long windows, which is 7.5±0.2 K/W, but it increases to 8.1 K/W for L_{win} of 1500 µm. The difference is possibly due to having a smaller laser section, which can impact the effective heat dissipation.

Figure 4.13 (b) presents the laser temperature (T_{las}) versus I_{las}. Again T_{las} values are calculated using equation 3.1. T_{las} increases with current more for the longer L_{win} designs. This is due to a smaller area of the laser section with the longer L_{win} leading to higher T_{las}.

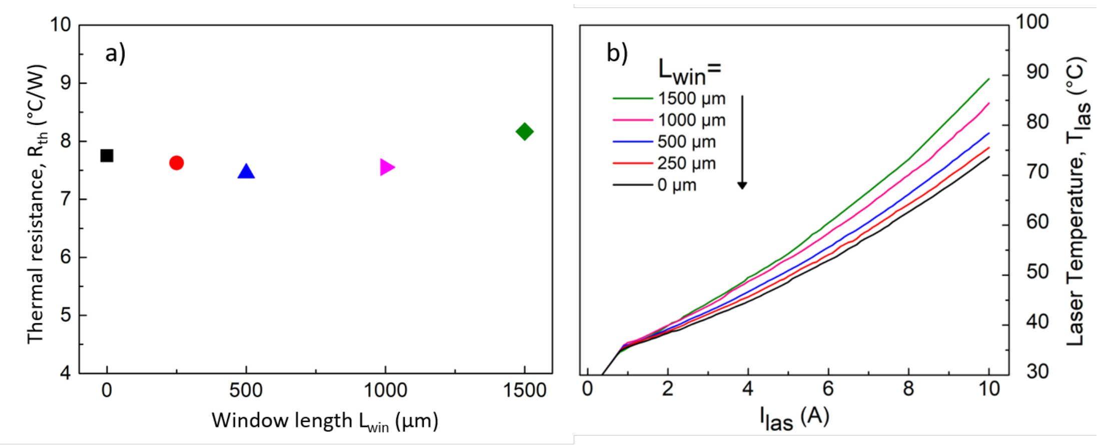

Figure 4.13: (a) Thermal resistance value of LDs studied in this work (b) Laser temperature of all LDs.

4.3.3 Facet temperature

After analyzing internal temperature for all the LDs, we characterized LDs facet temperature with I_{win}=0 and then analyzed how I_{win} affects their behavior. Figure 4.14 presents the temperature characterization results of the multi-section LDs and compares them with standard LD with I_{win}=0. Figure 4.14 (a) illustrates the structure of the multi-section LD, and the enlarged image corresponds to the waveguide temperature map of the laser with L_{win}=1000 µm. Figure 4.14 (b) shows the facet temperature maps of all the designs for a high operating current of I_{las}=10 A with I_{win}=0. The facet gets cooler with longer L_{win} due to the separation of the heat-generating laser region from the facet as depicted in figure 4.1. The heat spreads from the active region down toward the heatsink, and the slight asymmetry of the temperature maps between the right and left sides is due to the cooling configuration of the test setup.

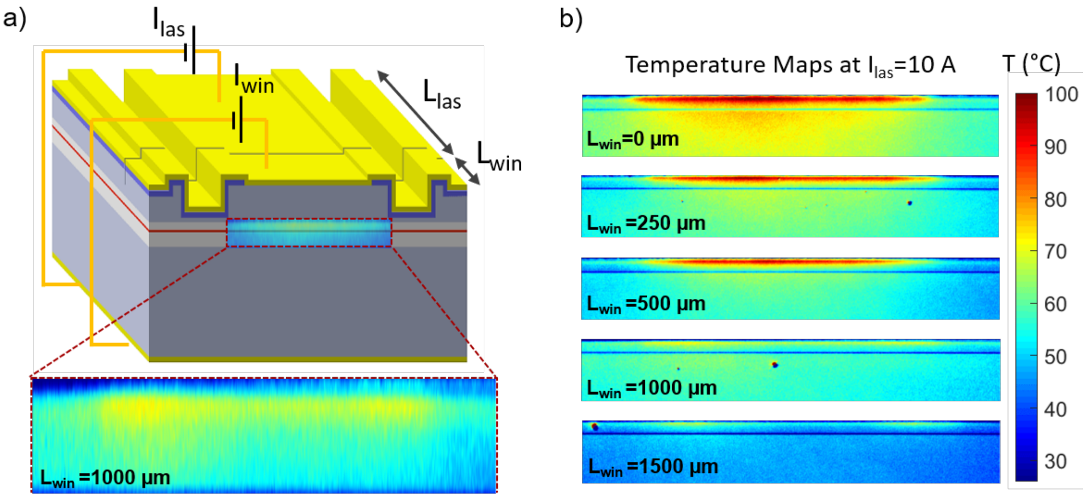

Figure 4.14: Comparison of temperature characteristics for all multi-section LDs at I_{las}=10 A and I_{win}=0. (a) LD structure and the enlarged image corresponding to the heated region of the facet for L_{win}=1000 µm. (b) temperature distribution maps.

Figure 4.15 shows the 2D zoomed view of the enlarged image in Figure 4.14 (a), depicting the detailed temperature map of the waveguide surface for LD with L_{win}=1000 µm at I_{las}=10 A without injecting I_{win}. The peak facet temperature, T_{fac}, is around 74 ℃, and it is lower than the laser temperature T_{las}= 85 ℃. Reaching a facet temperature lower than the laser junction temperature has been an optimistic goal for decades, which we achieved by exploiting our novel method. It is evident that the peak temperature on the facet for two-section LD with L_{win}=1000 µm (74 ℃) is much further away from the COMD critical temperature (120 - 150 ℃) compare to the peak facet temperature in standard single section structure (105 ℃) as shown in figure 3.7 making the device much more robust against COMD. The areas on the top left, and right side of the figure having cool temperature, corresponds to the trenches introduced in the fabrication process where we form waveguide (figure 4.3).

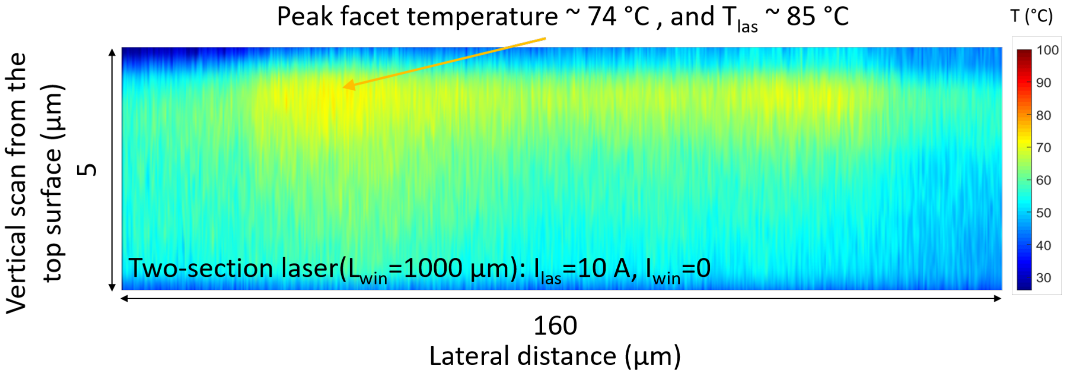

Figure 4.15: An enlarged view of the facet temperature map of the two section LD with L_{win}=1000 µm at I_{las} = 10A.

Figure 4.16 shows T_{fac} as a function of the distance from the top of the LD to the GaAs substrate (solid lines) and T_{las} (dashed lines). For T_{fac}, temperature values are average along the 40 µm width of the waveguide center. The peak in the temperature occurs around the quantum well active region and the surrounding layers, which is limited by the spatial resolution of the TR setup.

This peak is attributed to the self-heating of the LD, non-radiative recombination mechanisms, and facet absorption of the output light. A dip is positioned around 6 µm from the surface, which coincides with the substrate-epi interface. The dip is an artifact caused possibly by optical scattering in the substrate-epi interface and thermal expansion due to a large composition difference between the substrate and initial epitaxial layers resulting in a false reflection signal. Comparing Figure 4.14 (b) and Figure 4.16, it is essential to note that the heated area gets smaller with longer L_{win} even though the peak T_{fac} roughly coincides for L_{win}=0, 250, and 500 µm. Hence, one can conclude that L_{win} reduces the impact of heat on the LD facet even for the shortest L_{win} investigated here.

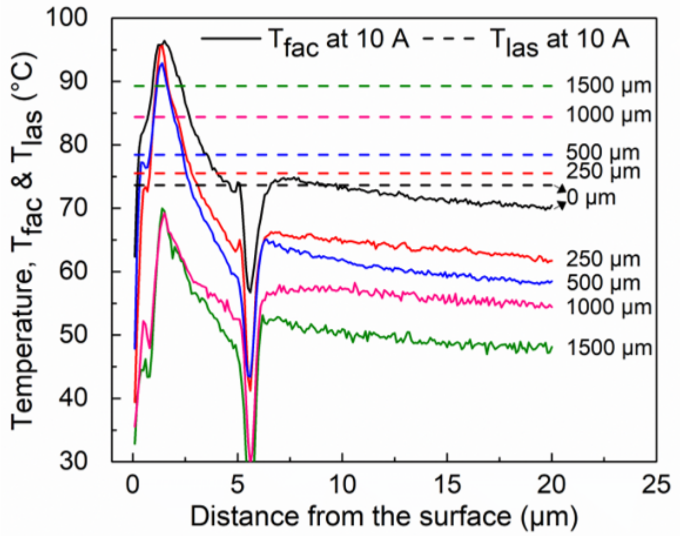

Figure 4.16: Vertical temperature scan of the figure 2-D temperature maps showing T_{fac} vs. distance from the top surface and T_{las} for I_{las}=10 A.

As demonstrated in Figure 4.16, the average and peak temperatures of the facet are lower than that of the standard LD (i.e., L_{win}=0) for all multi-section LDs. More importantly, even the peak T_{fac} is lower than T_{las} of any designs for L_{win} of 1000 and 1500 µm. Comparing these two designs show that the peak T_{fac} values are comparable for both, which indicates that L_{win} of 1000 µm is long enough to isolate the laser section heat from the facet. Due to this advantage, we select L_{win}=500 and 1000 µm for further investigation compared to standard LD as a reference.

In the above results, I_{win}=0 mA led to optical absorption losses due to the unpumped window section. In addition to the power degradation (Figure 4.7 (a)) of such configuration, the optical absorption of the window generates heat, as mentioned before. Therefore, the window section needs to be electrically pumped to overcome power losses and heating to decrease the junction temperature in the vicinity of the output facet. We show in the figure 4.9 that power is recovered by pumping the window section at the proper value. Next was investigating the facet temperature of LDs while pumping the window section. I_{win}=200 and 400 mA are selected as appropriate current levels for L_{win}=500 µm in order to get comparable output power to the standard laser. Similarly, I_{win}=400 and 800 mA are set for the LD with L_{win}=1000 µm. Figure 4.17 compares T_{fac} of LDs with L_{win}=500 and 1000 µm at I_{las}=4 A. Injecting I_{win} reduces the facet temperature for both LDs at both I_{las} values. This result agrees with Figure 4.10 since improved output with I_{win} injection reduces the heat generation of the laser in the window region, resulting in lower temperatures. The output power and T_{fac} results confirm that pumping the window section at proper I_{win} conditions provides effective recovery of the power degradation and further cooling of the LD facet.

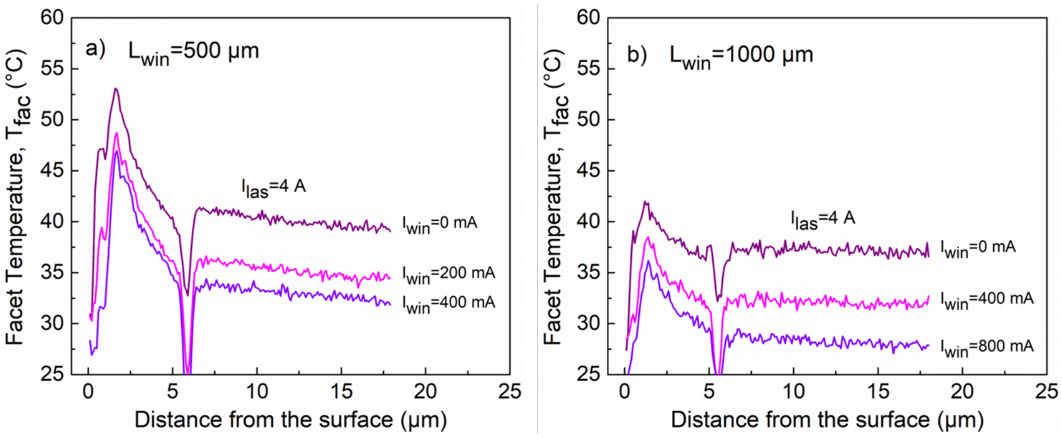

Figure 4.17: Facet temperature comparison of multi-section LDs at I_{las} = 4 A for (a) L_{win} = 500 µm with I_{win} = 0, 200, 400 mA, and (b) L_{win} = 1000 µm with I_{win} = 0, 400, 800 mA.

Figure 4.18 shows a comprehensive comparison of all the LDs investigated in this work where peak facet temperature, $T_{fac,peak}$, is plotted as a function of I_{las} for I_{win}= 0A. At all currents, the standard LD (L_{win}=0) has the highest $T_{fac,peak}$. The LD with L_{win}= 1000 µm has the lowest $T_{fac,peak}$ as it can be seen.

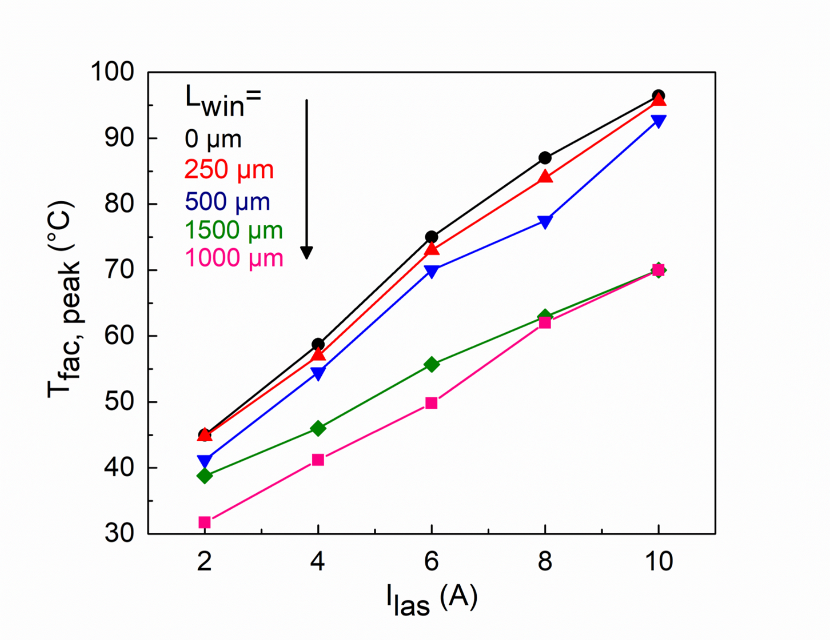

Figure 4.18: Peak facet temperature, $T_{fac,peak}$, versus I_{las} comparison of all LDs studied in this work.

4.3.4 COMD test

Next, we implemented a high current test and failure analysis for the LDs based on the above results as we did for the standard LD, section 3.1.4, and compared them. Figure 4.19 demonstrates the CW L-I curves up to I_{las}=20 A, and Figure 4.20 presents the laser facet image and top view of the laser cavity electroluminescence (EL) for the failed LDs. Figure 4.19 demonstrates the test results of three LDs with different I_{win} to see how the multi-section designs affect the performance and COMD threshold at high current. The TEC temperature is set as 20 °C for the test to reduce the thermal effects caused by the epi-up assembly. The maximum power and corresponding current of the L_{win}=0 µm design are 13.1 W and 14.5 A, respectively. A COMD point is apparent in the epitaxial layer, as shown in Figure 4.20 (a1). The top EL image in figure 4.20 (a2) demonstrates that the dark line defects (DLDs) extend from the "COMD point" on the front facet towards the laser cavity, which is a typical COMD behavior [11]. For L_{win}=500 µm with I_{win}=400 mA, the maximum power (current) is 13.6 W (15.5 A), which is 0.5 W (1 A) higher than that of L_{win}=0 µm LD. Figure 4.20 (b1) shows that the front facet looks clear without any apparent COMD blister under optical microscopy. The EL image shows that it is catastrophic optical bulk damage (COBD) in the laser section and separated from the window section as shown in figure 4.20 (b2). The DLDs originate from two points and extend into the laser cavity.

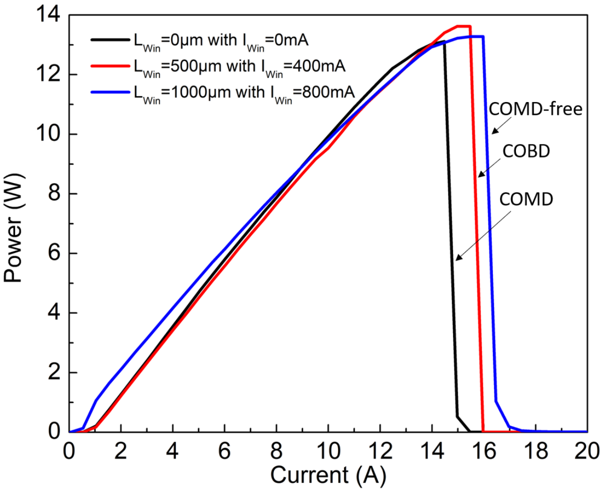

Figure 4.19: L-I curves for three different LDs under CW operation at 20℃.

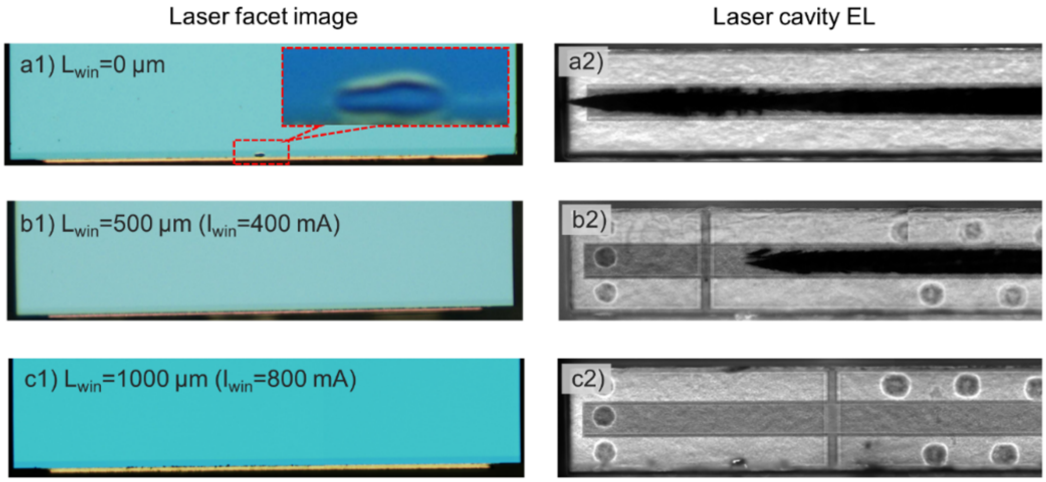

Figure 4.20: Optical microscope image of the laser facet and top EL image of the laser cavity after 20 A, CW, 20 ℃overdrive tests: (a1-2) L_{win} = 0 µm, (b1-2) L_{win} = 500 µm, (c1-2) L_{win} = 1000 µm.

For L_{win}=1000 µm with I_{win}=800 mA, the maximum power is 13.4 W at 16 A. The maximum current of this LD is 1.5 A larger than that of L_{win}=0 µm LD. Then, the output drops to zero without any sign of COMD. This LD was retested several times, showing no sign of power degradation. Figure 4.20 (c1-c2) shows the laser output facet and internal structure confirming that the LD operation is COMD-free. Under these optimized conditions, the multi-section LDs with L_{win}=500 and 1000 µm show similar output power levels to the standard LD (L_{win}=0). However, multi-section LDs have higher current densities and higher T_{las} for a given I_{las} due to the shorter L_{las} since the total length is the same for all LDs. The higher current densities of multi-section LDs make them more vulnerable to COBD, as shown for L_{win}=500 µm, but COMD-free operation is confirmed for both window lengths. LDs can be designed to have a fixed L_{las} section, and L_{win} are added as a cooling section, which would improve their reliability against COBD. Additionally, regular epi-down assembly of these high-power chips would reduce T_{las} even further. This combination would improve the COBD-free operation range of the multi-section LDs.

Chapter 5

Multi-section waveguide method for narrow waveguide and arrays

So far, we have investigated the single multi-section LD performance and made a full comparison with a standard LD in their LIV, output facet temperature, and COMD results. Also, we compared the performance and characteristics of a narrow waveguide (7 µm) LD with a standard broad-area (100 µm) LD. Having the idea of these measurements and results, we decided to implement and investigate the multi-section method in narrow waveguide LDs (25 and 50 µm) and their arrays where we have a fixed emission area (200 µm). We compared them with single and array LDs having 100 µm waveguide width to see how the multi-section method would affect their performance and whether we still would have the same cooling effect on the output facet.

5.1 Device design

Figure 5.1 shows the mask layout and design variations where we have 4 mm single section and 5 mm (L_{las}=4 mm, L_{win}=1 mm) two-section LDs. The emission area in all array lasers is 200 µm with a 50 % fill factor. We have a single and an array waveguides with 10, 25, 50, and 100 µm widths in sections (a), (b), (c), and (d), respectively.

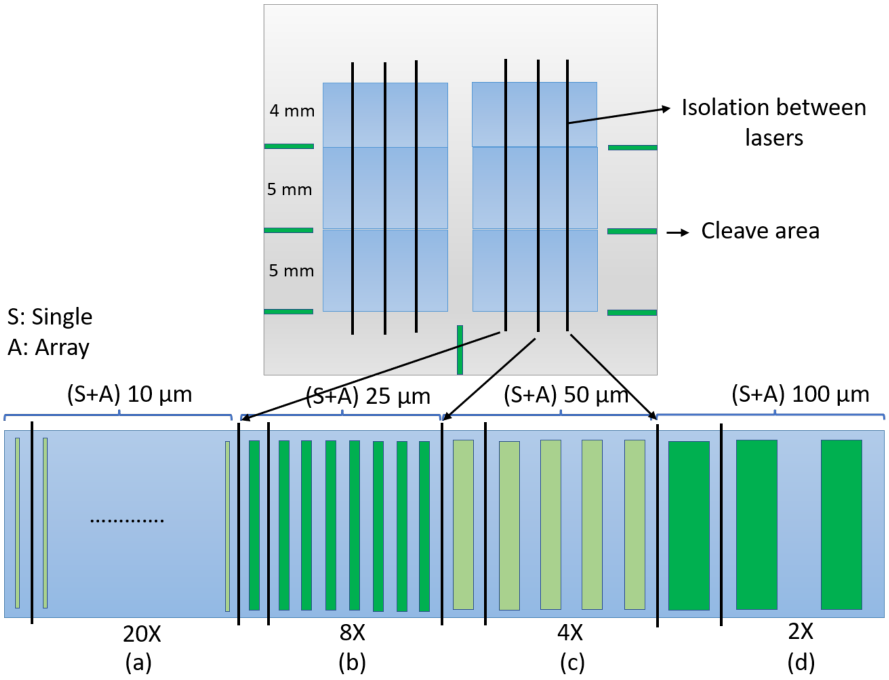

Figure 5.1: device design

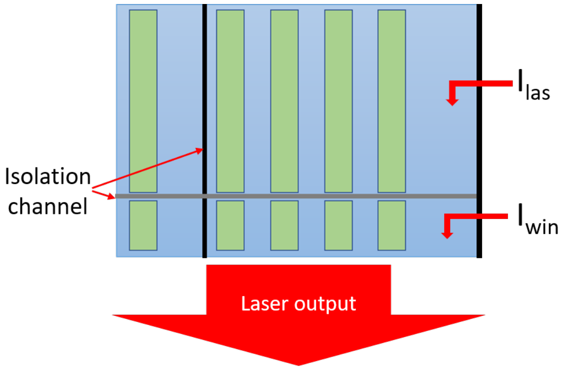

Figure 5.2: Schematic description of the multi-section single and array LDs.

5.2 Fabrication

5.2.1 Mask Layout

Photomask fabrication is the first step in device fabrication, and it is a costly and complex process that needs to be done carefully. Mask is used to transfer patterns in optical lithography, which is the dominant patterning technology in micro-fabrication. Figure 5.3 shows a general view of the mask's design.

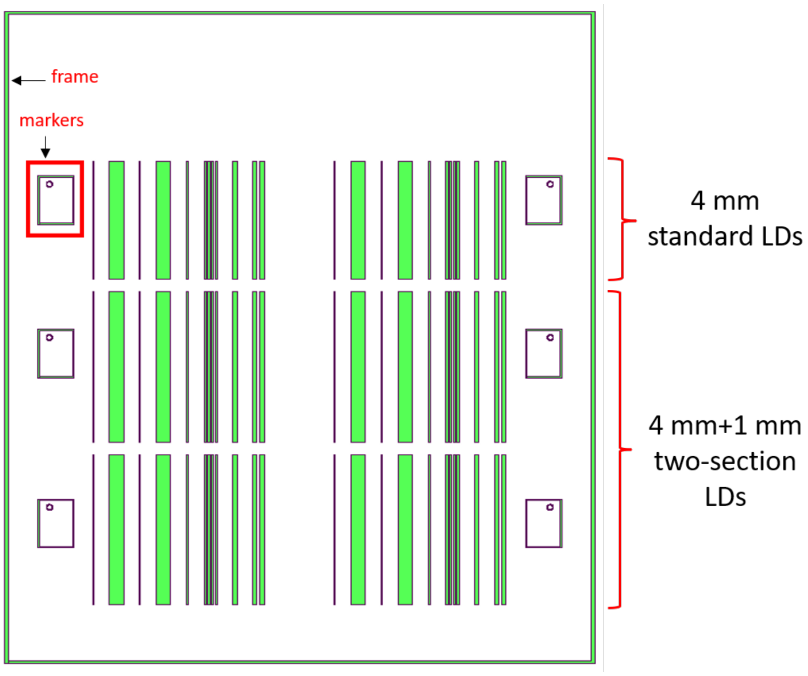

Figure 5.3: General view of the mask design.

Alignment of the sample is the most challenging step in doing optical lithography. We use the frame and markers shown in the figure 5.3 to do alignment at each step. The frame is used for the rough alignment and markers for the fine alignment. In this project, we have seven masks which means we need to do six alignment processes.

5.2.2 Process

Figure 5.4 shows the outline of the standard fabrication process for the device fabrication.

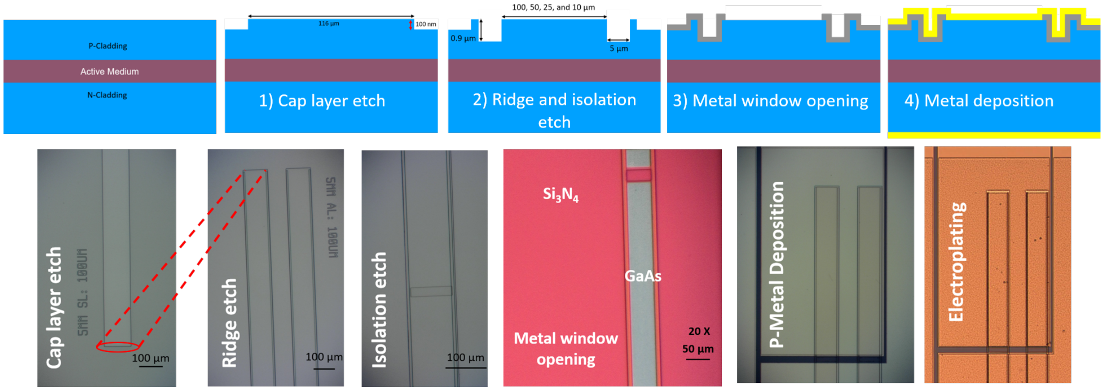

Figure 5.4: (1) Cap layer etch (2) Ridge and isolation etch (3) P-metal window opening (4) P-metal deposition.

Cap layer etch

We have 100 nm of highly doped GaAs cap layer in the epitaxial design. We get the cap layer via chemical etching by diluting phosphoric acid with hydrogen peroxide. Wafer oxidizing is done by hydrogen peroxide in the etchant solution. Subsequently phosphoric acid does the etching of highly doped GaAs in 20 seconds to remove the 100 nm cap layer shown in the figure 5.5. We also used the same solution for the ridge and isolation channel etch steps.

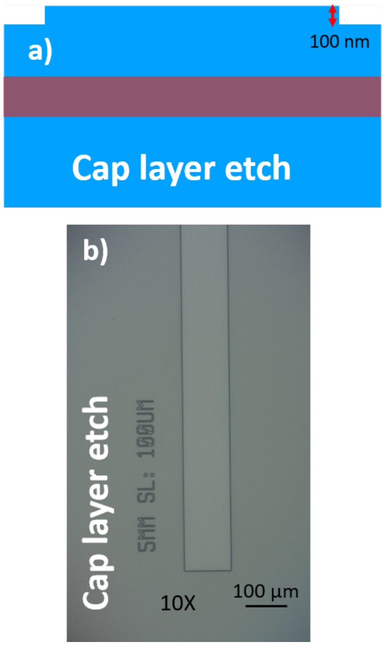

Figure 5.5: (a) Schematic of out put facet after cap layer etch. (b) Top view of the device after cap layer etch taken by optical microscopy with 10x lens.

Ridge and isolation channel etch

Figure 5.6 (a) and (c) show the schematic of the facet and top view of the device after the ridge etch step, respectively, where we define the ridges creating the refractive index difference for optical mode confinement. Near the output facets, we have a 100 µm long unpumped window, which is visible in the figure 5.4 in the electroplating image.

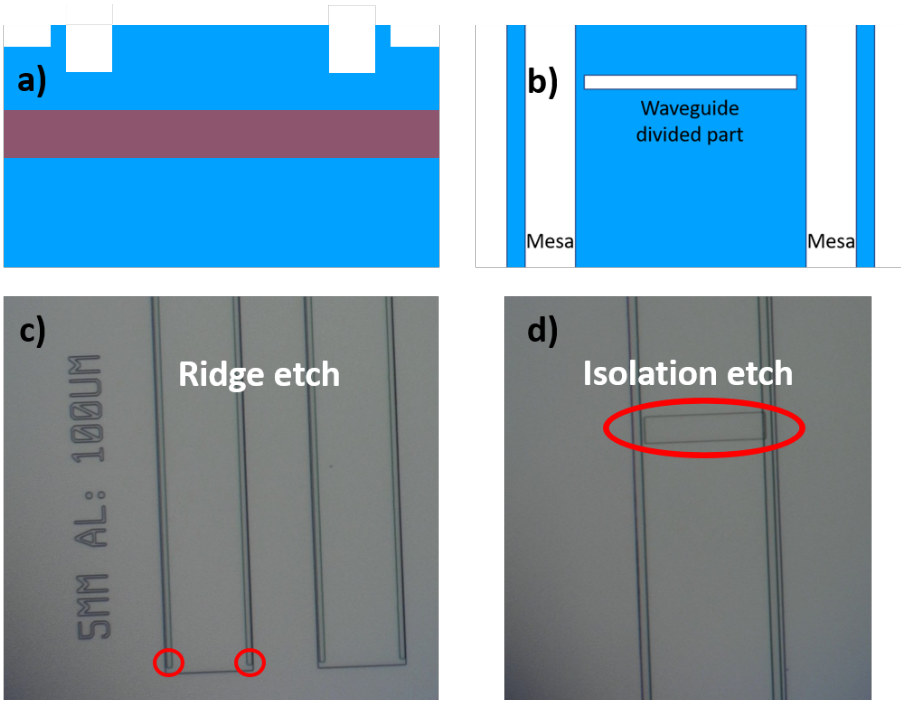

Figure 5.6: (a) Schematic of facet after mesa etch. (b) Top view Schematic of the waveguide after mesa, and waveguide dividing etch steps (c) Top view of the device after mesa etch taken by optical microscopy (d) Top view of the device after waveguide dividing etch taken by optical microscopy.

Figure 5.6 (b) and (d) show the top view schematic and optical microscope image of the ridge and isolation etch steps, respectively. In isolation etch step, we divide the waveguide into two-section, laser and window sections by 500 nm deep etching.

P-metal window opening

We use PECVD deposited silicon nitride (Si_3N_4) as the electrical isolation layer not to inject current outside the waveguide. Ridge is also covered by the dielectric after the silicon nitride deposition step. Next, we used BOE etchant to etch the dielectric and open the waveguide, as shown in figure 5.7 (b).

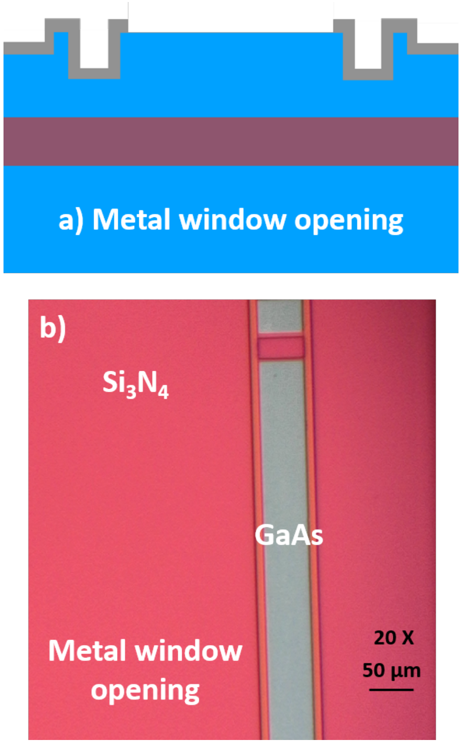

Figure 5.7: (a) Facet view of the structure after window opening. (b) Optical microscopy image from the top after window opening, red area is silicon nitride, and white area is the window opening.

The most important detail here is the area where we are dividing the waveguide, as it is clear in the figure 5.7 (b). The ridge dividing the waveguide into two-section must be covered with the dielectric to make them electrically isolated from each other.

Metal contacts deposition

We deposit two metal layers as top contact (p-metal) and bottom contact (n-metal). This step is crucial in our device fabrication to define the window and laser section, and they need to be electrically isolated from each other. Figure 5.8 (b) shows the top view of the laser after the p-metal deposition step allowed by the liftoff process. It is obvious that the window section is isolated from the gain section with the dielectric material (darker areas), where the bright region is the deposited gold.

Gold (Au) is used as the contact metal due to its superior performance, such as high electrical conductivity and resistance to corrosion. However, it has poor adhesion to the GaAs surface. As a result, 20 nm Ti (Titanium) is deposited using an e-beam deposition machine on the GaAs substrate as an adhesion layer. Next, Pt (Platinum) layer is deposited with an e-beam deposition machine to stop gold diffusion during the annealing process. Finally, a 120 nm AU layer is deposited by e-beam deposition. Through the lift-off process, we can separate LDs from each other and the window from the laser section. Image reversal lithography is used to have a PR structure suitable for the lift-off process.

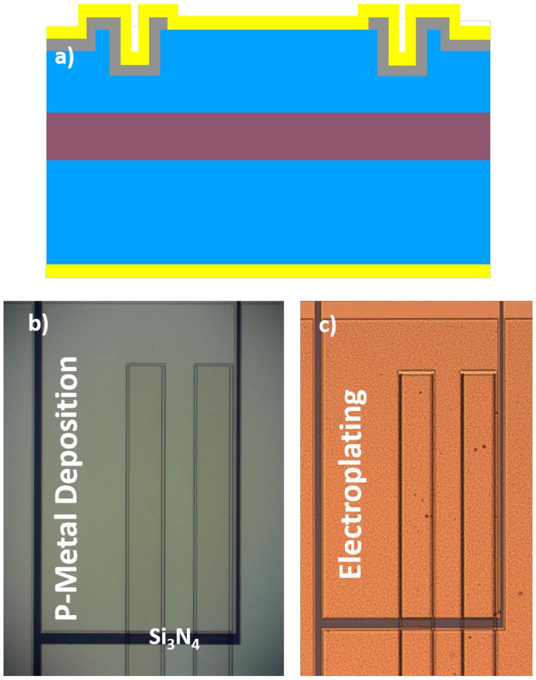

Figure 5.8: (a) Schematic of the facet view after metal deposition (b) Top view optical microscopy picture after p-metal deposition (c) Top view optical microscopy image after electroplating (1.4 µm gold).

To enable uniform current injection, we deposited 1.4 µm extra gold via electrochemical deposition, figure 5.8 (c).

Isolation and cleave

Isolation of the LDs from each other is essential for testing without singulation. We use chemical etching to isolate LDs. In our structure, the substrate starts after ˜ 5 µm from the top, so 10 µm seep etch is enough for isolation.

We also create 10 µm deep cleaving marks during this step to guide the diamond tip for cleaving.

5.3 Characterization

We used the setup described in chapter four, figure 4.5, to do laser characterization.

5.3.1 Performance

We investigated our single and array lasers having 25, 50, and 100 µm wide waveguides for their electro-optical performance and temperature characteristics. First, we checked the resistance between LDs to ensure that they were isolated from each other. To do so, we probed to each side of the isolation area and measured the current while changing voltage, as shown in the figure 5.9 (a). The resistance value between LDs is in the order of $M\Omega$, confirming that they are isolated from each other.

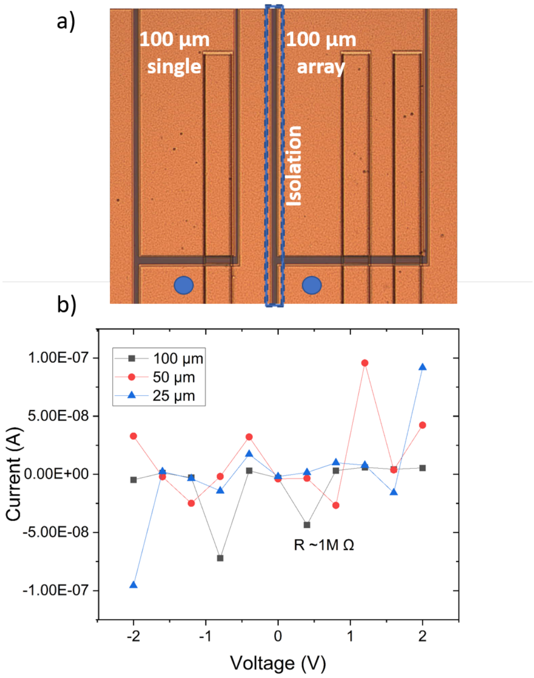

Figure 5.9: (a) Top view of the 100 µm single laser and array laser with isolation gap in between. (b) I-V between LDs.

Next, we measured the resistance between the laser and window section for each design. The resistance between the sections needs to be high enough to ensure that there is no leakage from the laser section to the window section. Figure 5.10 shows the resistance value between the sections for each design. Measured resistance values higher than 100 Ω indicates that we will not have a leakage issue while injecting current on the laser section.

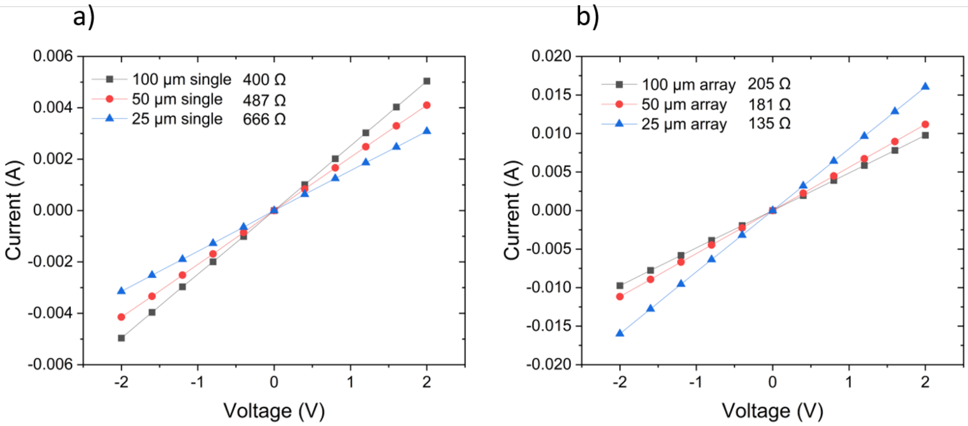

Figure 5.10: Resistance value between gain section and transparent window for (a) single lasers (b) array lasers.

After confirming that we don't have any leakage in our device, we measured the output optical power of the LDs. We set a specific current limit for each design based on the output emission area. For the 100 µm waveguide single LD, the current limit is chosen to be 4 A, and we scaled it for the other designs such as 2 A, 1 A for 50 µm, and 25 µm, respectively, and 8 A for all the array lasers since the output emission area is fixed at 200 µm for the arrays. Figure 5.11 shows the LI characteristics of the LDs. The threshold current is 0.15, 0.25, and 0.6 A for the 25 µm, 50 µm, and 100 µm single LDs, respectively, and it is 1.15 A for all the array lasers. The threshold current has roughly a linear relationship with the LD waveguide width.

As it can be seen from the figure 5.11 (b), the output power for the array lasers having different waveguide widths is almost the same due to the fact that they all have the same emission area (200 µm).

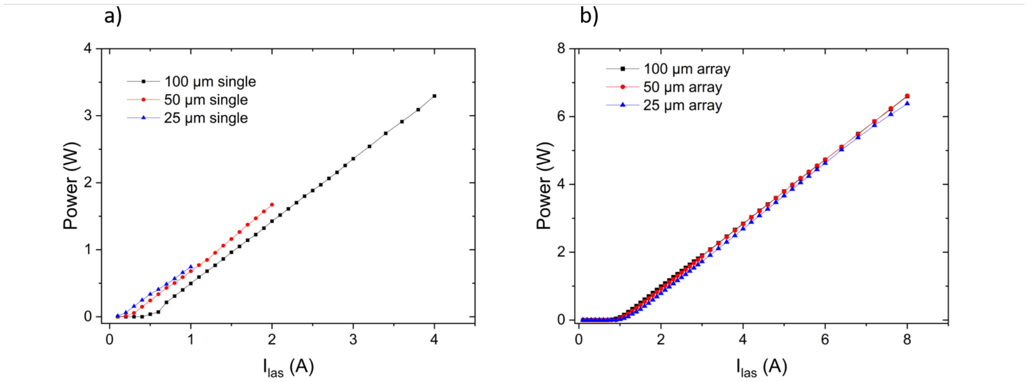

Figure 5.11: LI characteristics (a) Single lasers (b) Array lasers.

Figure 5.12 demonstrates the I-V characteristic for each design under CW operation at 20 ℃. In figure 5.12 (a), single LDs have different IV characteristics due to having different waveguide widths. The lower the injection area, the higher the resistance, as seen from the slope of the graphs in (a). However, in figure (b), array LDs have similar IV characteristics resulting from having the same total emission area.

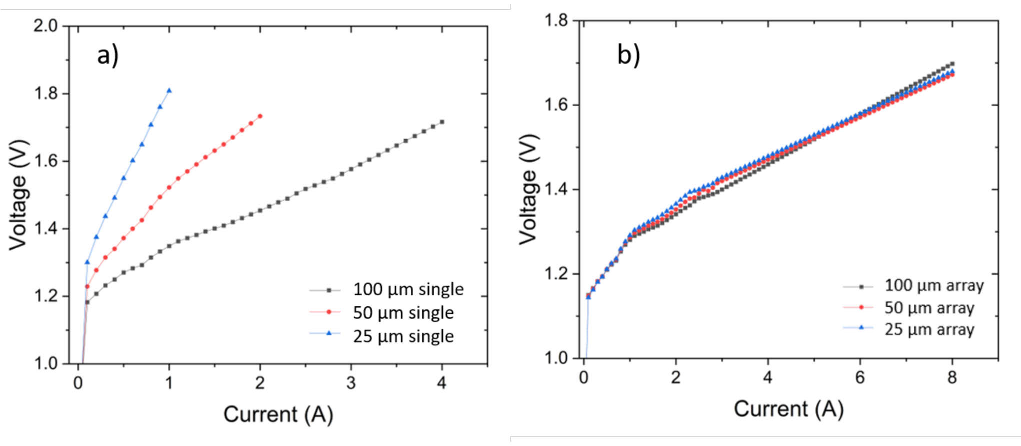

Figure 5.12: IV Characteristics of (a) single lasers, and (b) array lasers.

5.3.2 Internal temperature

As described in section 3.1.2, we can measure LD internal temperature using equations 3.1, 3.2, 3.3, by using laser LIV data. As mentioned in the previous sections, first we need to find R_{th}, and based on equation 3.3 we need $\Delta\lambda/\Delta P_{waste}$ and $\Delta\lambda/\Delta T$ values.

To find $\Delta\lambda/\Delta T$ value, we did measurement as described in 3.1.2 and slope of the curves in figure 5.13 is $0.33 nm/°C$. Moreover, since the laser is biased using a current source with PW=500 ns and 0.5 % d.c., there is almost no heat generated inside the devices. Both 100 and 25 µm width LDs have the same value, confirming that $\Delta\lambda/\Delta T$ is a material property.

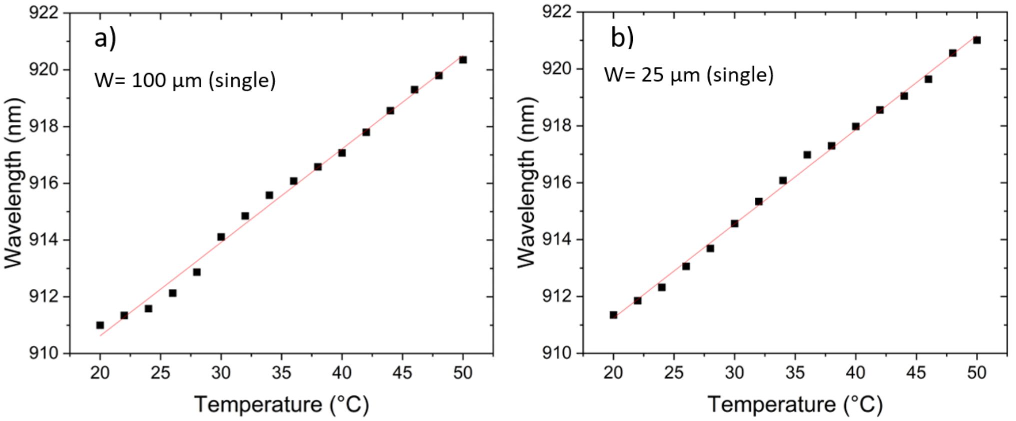

Figure 5.13: Wavelength variation with temperature at 3A and 2A for (a) 100 µm single laser (b) 25 µm single laser, respectively.

To find $\Delta\lambda/\Delta P_{waste}$ we implemented measurement as described in 3.1.2. Then we plot wavelength as a function of waste heat for each LD separately, as demonstrated in figure 5.14.

Slopes of the curves in the figure 5.14 are 2.9, 3.7, 2.7, 2.3, 2.4, 2.1 nm/W for 25 µm single, 50µm single, 100 µm single, 25 µm array, 50 µm array, 100 µm array lasers, respectively.

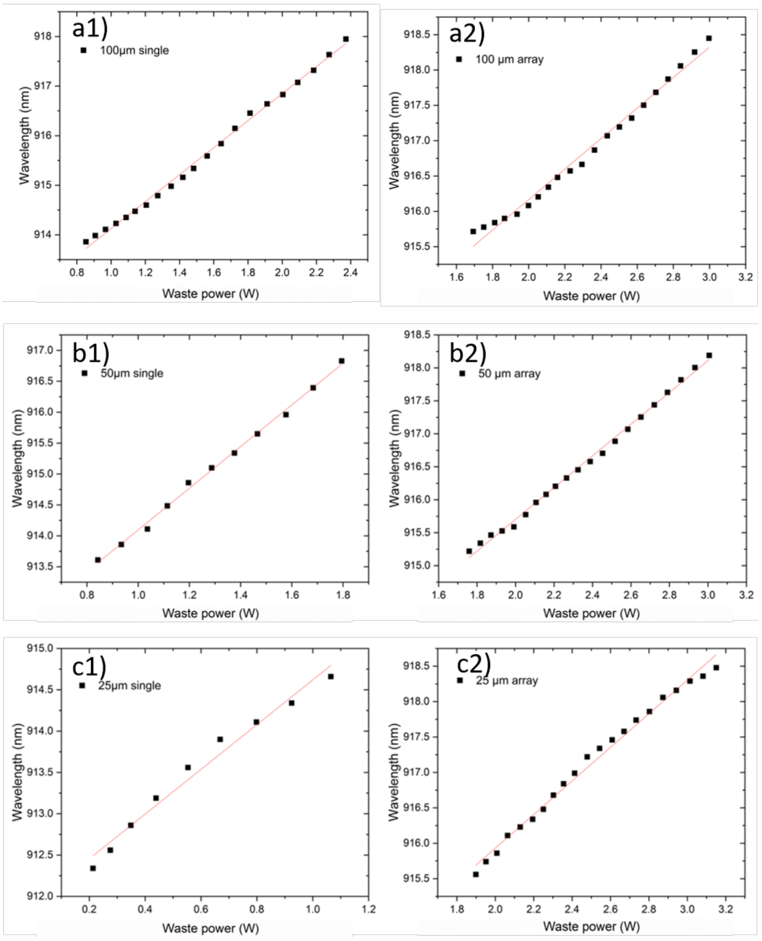

Figure 5.14: Graphs of wavelength variation with wast power at fixed temperature= 20 °Cfor (a1, a2) 100 µm single and array. (b1, b2) 50 µm single and array. (c1, c2) 25 µm single and array.

Calculated R_{th} value for these LDs is shown in the figure 5.15. For single LD, the R_{th} is smaller for a narrow waveguide compared to a wide waveguide. However, since we had a few LD to do testing, we couldn't get an acceptable trend that needs further investigations. On the other side, R_{th} is comparable for the array LDs with different waveguide widths (7 ± 0.5 K/W) as anticipated.

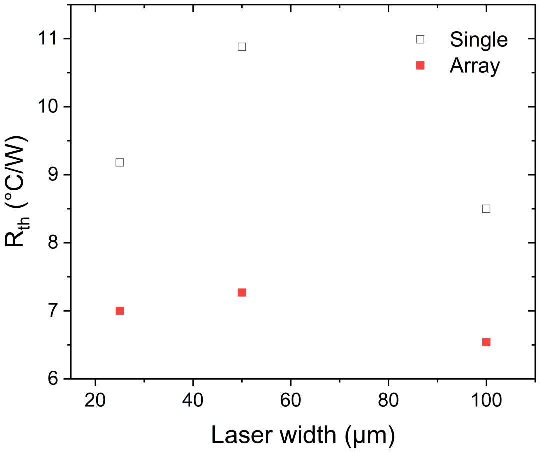

Figure 5.15: Thermal resistance value of LDs

Figure 5.16 presents the lasers temperature (T_{las}) versus I_{las}. Again T_{las} values are calculated using equation 3.1. Although the T_{las} is lower for the narrow waveguide LD as shown in figure 5.16 (a), the heat load density is much higher for them compared to 100 μm wide waveguide LD. Figure 5.16 (b) presents the T_{las} for the array LDs, which indicates they have almost the same laser temperature and the slight difference for the 100 μm wide waveguide array LD is due to a smaller R_{th}.

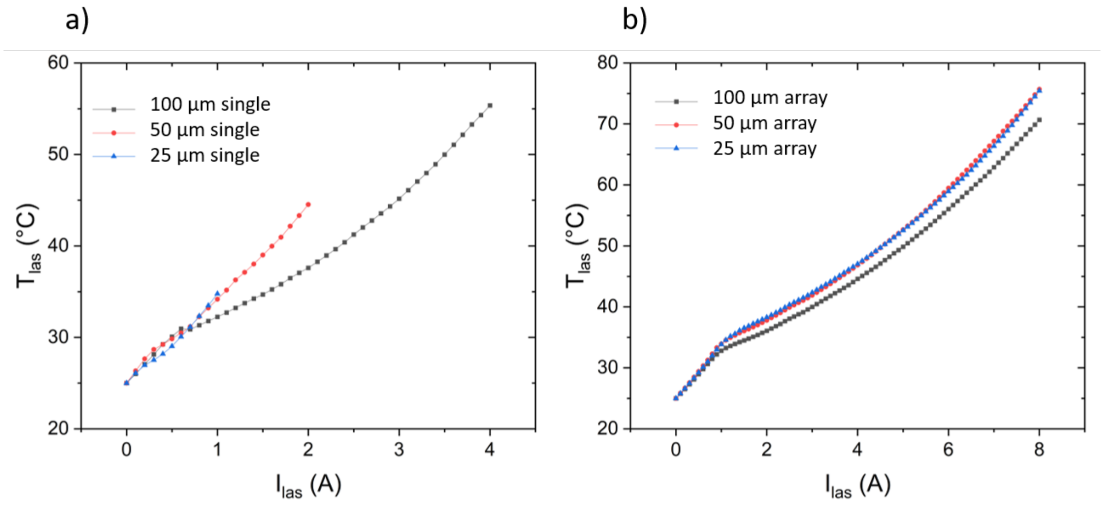

Figure 5.16: Laser temperature of all LDs (a) single lasers, and (b) array lasers

5.3.3 Facet temperature

After doing a full performance characterization for all the LDs, we characterized single waveguide LDs' facet temperature with I_{win}=0 and then analyzed how I_{win} affects their behavior. LDs are biased at the same current density levels to make them comparable. Moreover, their output power density for the selected current is the same. We choose I_{las}= 4A for the 100 µm width LD. Therefore, 50 and 25 µm width LDs are biased at I_{las}= 2 and 1 A to have the same current densities. Figure 5.17 presents the temperature characterization results of the two-section single LDs with different widths of 100, 50, and 25 µm at I_{win}=0 A, with I_{las}=4, 2, and 1A current, respectively. Figure 5.17 (a) shows the facet temperature maps of all the single emitters at the operating current with I_{win}=0. There is an artifact in the temperature map of the 100 µm waveguide LD presented in figure 5.17 (a), some p-metal lifted up close to the facet and caused a partial shading on the laser facet. This affects the thermoreflectance signal in the shaded area but not the center of the laser output facet where the averaging scan is applied.

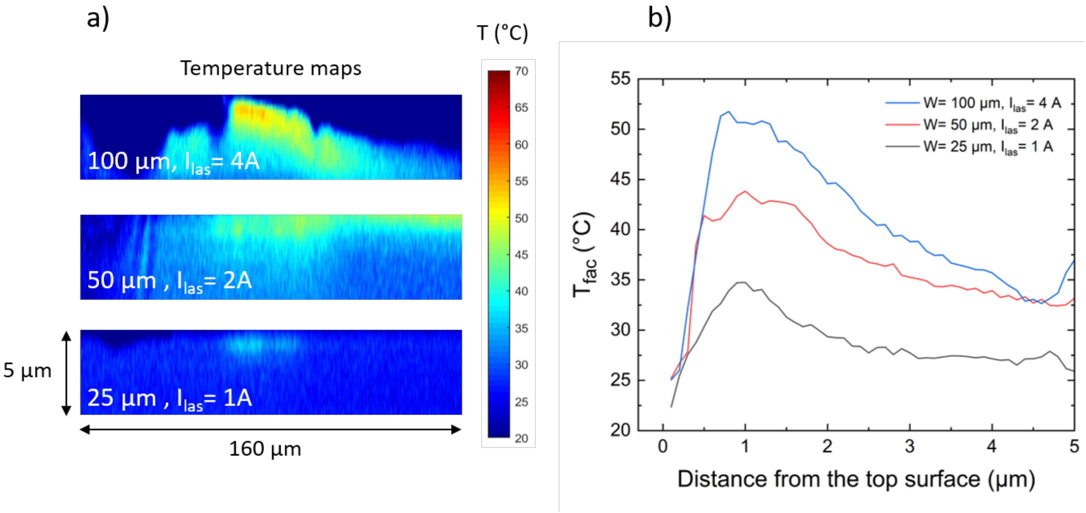

Figure 5.17: Comparison of facet temperature for all single waveguide two-section LDs at I_{las}=4, 2, and 1 A with I_{win}=0 at T=24 °C. (a) Facet temperature maps. (b) Vertical temperature scan of the temperature maps.

Although all single emitters have the same output power density, injecting current density and internal heat density, the facet temperature is lower for the smaller width LDs. This is a sign of better heat dissipation for the narrower waveguide LD. Figure 5.17 (b) is a vertical scan of facet temperatures showing T_{fac} as a function of the distance from the top of the LDs. For T_{fac}, temperature values are averaged along the 25 µm center of the waveguide width. It clearly shows that the peak facet temperature for the 25 µm width laser is much lower compared to the LDs with 100 and 50 µm waveguides.

In the above results, I_{win}=0 mA led to optical absorption losses due to the unpumped window section. In addition to the power degradation of such configuration, the optical absorption of the window generates heat, as mentioned before. Therefore, the window section needs to be electrically pumped to overcome power losses and heating to decrease the junction temperature around the output facet. Then, we investigate the facet temperature of LDs while pumping the window section at an equal current density level, as mentioned before. I_{win}=100, 50, and 25 mA are selected as appropriate current levels for lasers with 100, 50, and 25 µm width, respectively, in order to get comparable output power density and same current density for the window section. Figure 5.18 presents the temperature characterization results of the multi-section single LDs with different width of 100, 50, and 25 µm with injecting I_{win}. I_{las} current is the same as before for each emitter. Figure 5.18 compares T_{fac} of LDs with width of 100, 50, and 25 µm at I_{las}=4, 2, and 1 A, respectively. Injecting I_{win} reduces the facet temperature for LDs at I_{las} values. Injecting I_{win} reduces the heat generation in the window region, resulting in lower temperatures. Comparing figure 5.18 with 5.17, one can see the temperature reduction clearly. 5.18 (a) shows the facet temperature maps of all the single emitters at operating current with I_{win}= 100, 50, and 25 mA. In (a), for the 100 µm waveguide width, we have the same shading issue on the output facet, as explained before.

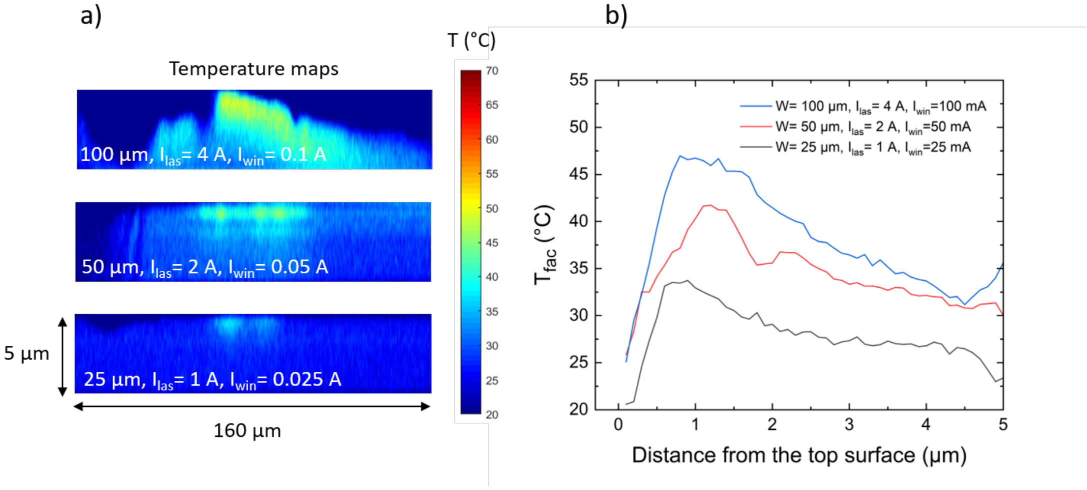

Figure 5.18: Temperature characterization results of the two-section single waveguide LDs with I_{win} (a) Temperature maps. (b) Vertical temperature scan of the temperature maps.

Figure 5.18 (b) is a vertical scan of facet temperatures in (a) showing T_{fac} as a function of the distance from the top of the LDs for the first 5 µm, corresponding to the waveguide area. For T_{fac}, temperature values are averaged along the 25 µm center of the waveguide width. Comparing with 5.17 (b), after injecting I_{win} for the 100, 50, and 25 µm waveguide width laser, we see 5, 2.5, and 1 ℃ reduction in the peak facet temperature. Therefore, these results prove that the multi-section method is also favorable for narrow waveguide lasers.

Next, we checked facet temperature maps of the array lasers with different waveguide widths of 100, 50, and 25 µm at I_{las}= 7A. As explained in the device structure section, all designs have the same total emission area. Their output power at chosen current is the same (6 W at I_{las}= 7A) as it can be seen from the figure 5.11 (b). As a result, all of them will have the same power density on the output facet. First, we started characterizing LDs facet temperature with I_{win}=0 and then analyzed how I_{win} affects their behavior.

Figure 5.19 presents the temperature characterization results of the multi-section array LDs with different width of 100, 50, and 25 µm at I_{win}=0 and I_{las}=7 A. Figure 5.19 (a) shows the facet temperature maps of all the array emitters. The result shows that 100 and 50 µm waveguide width array lasers have comparable temperature maps, and the 25 µm one has a slightly cooler facet. Figure 5.19 (b) is a vertical scan of facet temperatures showing T_{fac} as a function of the distance from the top of the LDs. For T_{fac}, temperature values are averaged along the 25 µm of the hottest spot on the facet. It shows that the peak facet temperature for the 25 µm width array laser is slightly lower than 100 µm broad area and 50 µm width array lasers.

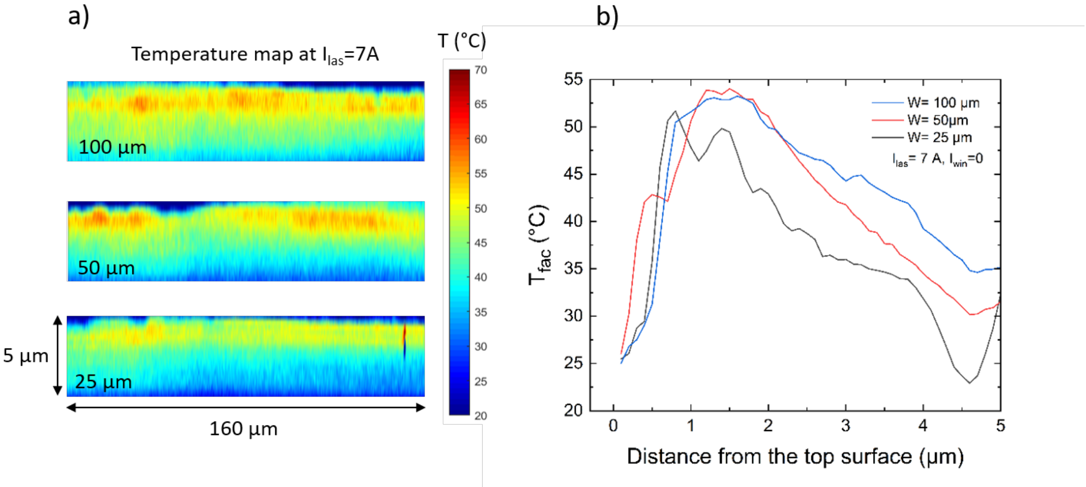

Figure 5.19: Temperature characterization results of the multi-section array LDs with I_{win} (a) Temperature distribution maps at I_{las}= 7A. (b) Vertical temperature scan of the temperature maps showing in (a) where T_{fac} plotted vs. distance from the top surface.

Then, we investigate the facet temperature of LDs while pumping the window section at equal current density levels for all. For the array lasers, the output emission area is 200 µm (2X single 100 µm single LD); therefore, the I_{win} value is chosen to be 200 mA.

Figure 5.20 presents the temperature characterization results of the multi-section array LDs with different width of 100, 50, and 25 µm at I_{win}=200 mA and I_{las}=7 A. Figure 5.20 (a) shows the facet temperature maps of all the array emitters. The result shows that all array lasers have comparable temperature maps. Figure 5.20 (b) is a vertical scan of facet temperatures showing T_{fac} as a function of the distance from the top of the LDs. For T_{fac}, temperature values are averaged along the 25 µm of the hottest spot on the facet. Compared with figure 5.19 (b), we can see close to 5 ℃ cooling due to 200 mA I_{win} injection. This again confirms the fact that the multi-section method is working for the array lasers as well.

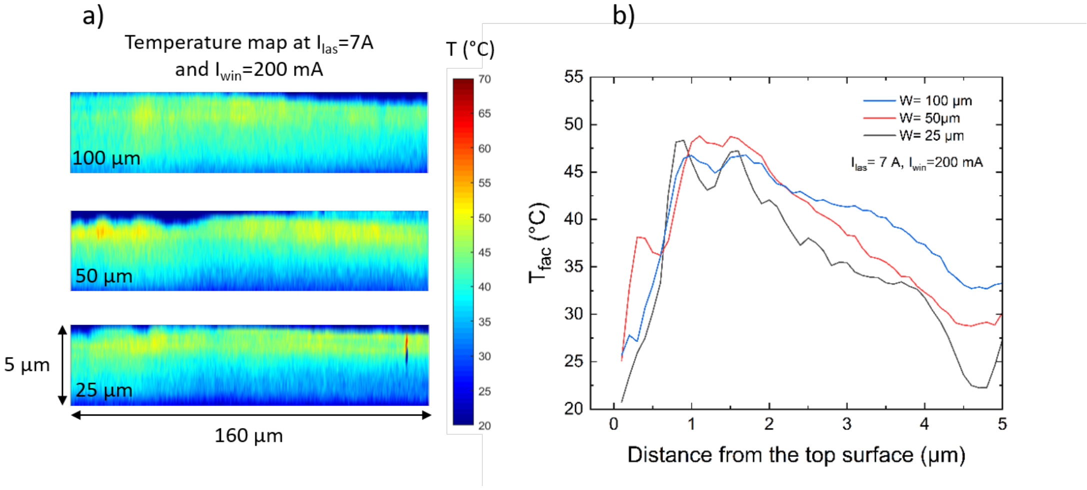

Figure 5.20: Temperature characterization results of the two-section array LDs with I_{win}=200mA (a) Temperature maps. (b) Vertical temperature scan of the temperature maps where T_{fac} plotted vs. distance from the top surface.

Chapter 6

Conclusion and outlook

In conclusion, first, we have addressed the dominant failure mode of LDs and experimentally demonstrated high-power edge-emitting LDs with COMD-free operation. In particular, by introducing a multi-section waveguide with laser and window sections separating the facet from the high heat-load of the laser, we were able to suppress the laser self-heating effect on the temperature-sensitive output facet. This, in turn, allows for high-power operation and dramatically reduced facet temperatures without COMD failure [33, 34]. The characteristics are confirmed by directly measuring the laser and output facet temperatures and the repeatable failure tests. These observations agree with the predictions in the literature based on the facet temperature impact on triggering the COMD failure mechanism. Next, we implement the multi-section method for single and array LDs with different waveguide widths to investigate how the multi-section method would affect the LD performance. The cooling effect is confirmed by directly measuring the laser output facet temperature. These results prove that the multi-section method is also favorable for narrow waveguide and array LDs improving their reliability.

Our work opens the door for exploring the multi-section waveguide approach in the long-term reliability improvement of semiconductor lasers with various material systems. Investigating the method with epi-down assembly and long-term reliability studies would be worthwhile. In the epi-down configuration, thermal resistance is lower than epi-up, and it helps to cool down LD better [54]. In this case, we expect to realize further cooling of the laser output facet and significant improvement in reliable output power and lifetime of these devices due to lower thermal resistance with epi-down assembly. An interesting question we would like to study in the future is “Can this concept be employed to push further the reliable output power operation limit of all high-power LDs and for different configurations?”. In particular, exploring multi-section LD design in high-power laser arrays would be interesting for improved reliability, and on-chip beam combining designs would be attractive. Multi-section LD would decrease the cost of sample size and maintenance of the system if it could push further the reliable output power operation limit of high-power LDs. Considering the slightly complicated operation and total cost, it is a balance to be considered whether it is a better choice in practice. We plan to address these questions in our future work.

Bibliography

[1] P. W. Epperlein, *Semiconductor laser engineering, reliability and diagnostics: a practical approach to high power and single mode devices.* John Wiley & Sons, 2013.

[2] J. I. Pankove, *Optical processes in semiconductors.* Courier Corporation, 1975.

[3] B. E. Saleh and M. C. Teich, *Fundamentals of photonics.* john Wiley & sons, 2019.

[4] W. W. Chow, S. W. Koch, and M. I. Sargent, *Semiconductor-laser physics.* Springer Science & Business Media, 2012.

[5] D. Pierścińska, "Thermoreflectance spectroscopy—analysis of thermal processes in semiconductor lasers," *Journal of Physics D: Applied Physics*, vol. 51, no. 1, p. 013001, 2017.

[6] E. Zucker, D. Zou, L. Zavala, H. Yu, P. Yalamanchili, L. Xu, H. Xu, D. Venables, J. Skidmore, V. Rossin, *et al.*, "Advancements in laser diode chip and packaging technologies for application in kw-class fiber laser pumping," in *High-Power Diode Laser Technology and Applications XII*, vol. 8965, pp. 38–51, SPIE, 2014.

[7] P. Crump, G. Erbert, H. Wenzel, C. Frevert, C. M. Schultz, K.-H. Hasler, R. Staske, B. Sumpf, A. Maassdorf, F. Bugge, *et al.*, "Efficient high-power

laser diodes," *IEEE Journal of Selected Topics in Quantum Electronics*, vol. 19, no. 4, pp. 1501211–1501211, 2013.

[8] H. Wenzel, P. Crump, A. Pietrzak, X. Wang, G. Erbert, and G. Tränkle, "Theoretical and experimental investigations of the limits to the maximum output power of laser diodes," *New Journal of Physics*, vol. 12, no. 8, p. 085007, 2010.

[9] M. Peters, V. Rossin, M. Everett, and E. Zucker, "High-power high-efficiency laser diodes at jdsu," in *High-Power Diode Laser Technology and Applications V*, vol. 6456, pp. 141–151, SPIE, 2007.

[10] Y. Zhao, Z. Wang, A. Demir, G. Yang, S. Ma, B. Xu, C. Sun, B. Li, and B. Qiu, "High efficiency 1.9 kw single diode laser bar epitaxially stacked with a tunnel junction," *IEEE Photonics Journal*, vol. 13, no. 3, pp. 1–8, 2021.

[11] A. Demir, M. Peters, R. Duesterberg, V. Rossin, and E. Zucker, "Semiconductor laser power enhancement by control of gain and power profiles," *IEEE Photonics Technology Letters*, vol. 27, no. 20, pp. 2178–2181, 2015.

[12] A. Demir, M. Peters, R. Duesterberg, V. Rossin, and E. Zucker, "29.5 w continuous wave output from 100um wide laser diode," in *High-Power Diode Laser Technology and Applications XIII*, vol. 9348, pp. 129–134, SPIE, 2015.

[13] V. Rossin, M. Peters, A. Demir, J. J. Morehead, J. Guo, Y. Xiao, J. Cheng, A. Hsieh, R. Duesterberg, and J. Skidmore, "High power, high brightness diode lasers for kw lasers systems," in *2015 IEEE High Power Diode Lasers and Systems Conference (HPD)*, pp. 35–36, IEEE, 2015.

[14] J. M. Pardell, R. Herrero, M. Botey, and K. Staliunas, "Non-hermitian arrangement for stable semiconductor laser arrays," *Optics express*, vol. 29, no. 15, pp. 23997–24009, 2021.

[15] P. Crump, G. Blume, K. Paschke, R. Staske, A. Pietrzak, U. Zeimer, S. Einfeldt, A. Ginolas, F. Bugge, K. Häusler, *et al.*, "20w continuous wave reliable operation of 980nm broad-area single emitter diode lasers with an aperture of 96um," in *High-Power Diode Laser Technology and Applications VII*, vol. 7198, pp. 315–323, SPIE, 2009.

[16] H. Wenzel, P. Crump, A. Pietrzak, C. Roder, X. Wang, and G. Erbert, "The analysis of factors limiting the maximum output power of broad-area laser diodes," *Optical and quantum electronics*, vol. 41, no. 9, pp. 645–652, 2009.

[17] P. Crump, H. Wenzel, G. Erbert, and G. Tränkle, "Progress in increasing the maximum achievable output power of broad area diode lasers," in *High-Power Diode Laser Technology and Applications X*, vol. 8241, pp. 222–231, SPIE, 2012.

[18] J. W. Tomm, M. Ziegler, M. Hempel, and T. Elsaesser, "Mechanisms and fast kinetics of the catastrophic optical damage (cod) in gaas-based diode lasers," *Laser & Photonics Reviews*, vol. 5, no. 3, pp. 422–441, 2011.

[19] M. Hempel, J. W. Tomm, M. Ziegler, T. Elsaesser, N. Michel, and M. Krakowski, "Catastrophic optical damage at front and rear facets of diode lasers," *Applied physics letters*, vol. 97, no. 23, p. 231101, 2010.

[20] M. Ziegler, M. Hempel, H. E. Larsen, J. W. Tomm, P. E. Andersen, S. Clausen, S. N. Elliott, and T. Elsaesser, "Physical limits of semiconductor laser operation: A time-resolved analysis of catastrophic optical damage," *Applied Physics Letters*, vol. 97, no. 2, p. 021110, 2010.

[21] M. Hempel, J. Tomm, M. Ziegler, T. Elsaesser, N. Michel, and M. Krakowski, "Catastrophic optical damage at front and rear facets of 975 nm emitting diode lasers," in *CLEO: Science and Innovations*, p. CTuP6, Optica Publishing Group, 2011.

[22] A. K. Jha, C. Li, K. P. Pipe, M. T. Crowley, D. B. Fullager, J. D. Helmrich, P. Thiagarajan, R. J. Deri, R. B. Swertfeger, and P. O. Leisher,

"Thermoreflectance-based measurement of facet optical absorption in high power diode lasers," *IEEE Photonics Technology Letters*, vol. 31, no. 24, pp. 1909–1912, 2019.

[23] J. Michaud, P. Del Vecchio, L. Béchou, D. Veyrié, M. A. Bettiati, F. Laruelle, and S. Grauby, "Precise facet temperature distribution of high-power laser diodes: Unpumped window effect," *IEEE Photonics Technology Letters*, vol. 27, no. 9, pp. 1002–1005, 2015.

[24] R. Lammert, J. Ungar, M. Osowski, H. Qi, M. Newkirk, and N. B. Chaim, "980-nm master oscillator power amplifiers with nonabsorbing mirrors," *IEEE Photonics Technology Letters*, vol. 11, no. 9, pp. 1099–1101, 1999.

[25] Q. Zhang, Y. Xiong, H. An, K. Boucke, and G. Treusch, "Unveiling laser diode "fossil" and the dynamic analysis for heliotropic growth of catastrophic optical damage in high power laser diodes," *Scientific reports*, vol. 6, no. 1, pp. 1–12, 2016.

[26] H. Naito, T. Nagakura, K. Torii, M. Takauji, H. Aoshima, T. Morita, J. Maeda, and H. Yoshida, "Long-term reliability of 915-nm broad-area laser diodes under 20-w cw operation," *IEEE Photonics Technology Letters*, vol. 27, no. 15, pp. 1660–1662, 2015.

[27] S. Arslan, A. Demir, S. Şahin, and A. Aydınlı, "Conservation of quantum efficiency in quantum well intermixing by stress engineering with dielectric bilayers," *Semiconductor Science and Technology*, vol. 33, no. 2, p. 025001, 2018.

[28] P. Ressel, G. Erbert, U. Zeimer, K. Hausler, G. Beister, B. Sumpf, A. Klehr, and G. Trankle, "Novel passivation process for the mirror facets of al-free active-region high-power semiconductor diode lasers," *IEEE Photonics Technology Letters*, vol. 17, no. 5, pp. 962–964, 2005.

[29] L. W. Tu, E. Schubert, M. Hong, and G. Zydzik, "In-vacuum cleaving and coating of semiconductor laser facets using thin silicon and a dielectric,"

Journal of applied physics, vol. 80, no. 11, pp. 6448–6451, 1996.

[30] P. Piva, S. Fafard, M. Dion, M. Buchanan, S. Charbonneau, R. Goldberg, and I. Mitchell, "Reduction of ingaas/gaas laser facet temperatures by band gap shifted extended cavities," *Applied physics letters*, vol. 70, no. 13, pp. 1662–1664, 1997.

[31] F. Rinner, J. Rogg, M. Kelemen, M. Mikulla, G. Weimann, J. Tomm, E. Thamm, and R. Poprawe, "Facet temperature reduction by a current blocking layer at the front facets of high-power ingaas/algaas lasers," *Journal of applied physics*, vol. 93, no. 3, pp. 1848–1850, 2003.

[32] M. Ziegler, V. Talalaev, J. W. Tomm, T. Elsaesser, P. Ressel, B. Sumpf, and G. Erbert, "Surface recombination and facet heating in high-power diode lasers," *Applied Physics Letters*, vol. 92, no. 20, p. 203506, 2008.

[33] K. Ebadi, Y. Liu, A. K. Sünnetçioglu, S. Gündogdu, S. Şengül, Y. Zhao, Y. Lan, G. Yang, and A. Demir, "Multisection waveguide method for facet temperature reduction and improved reliability of high-power laser diodes," in *Semiconductor Lasers and Laser Dynamics X*, vol. 12141, pp. 12–20, SPIE, 2022.

[34] Y. Liu, K. Ebadi, A. K. Sunnetcioglu, S. Gundogdu, S. Sengul, Y. Zhao, Y. Lan, Y. Zhao, G. Yang, and A. Demir, "Elimination of catastrophic optical mirror damage in continuous-wave high-power laser diodes using multisection waveguides," *Optics Express*, vol. 30, no. 18, pp. 31539–31549, 2022.

[35] S. Arslan, S. Gündoğdu, A. Demir, and A. Aydınlı, "Facet cooling in high-power ingaas/algaas lasers," *IEEE Photonics Technology Letters*, vol. 31, no. 1, pp. 94–97, 2018.

[36] A. Demir, S. Arslan, S. Gündoğdu, and A. Aydinli, "Reduced facet temperature in semiconductor lasers using electrically pumped windows," in *High-Power Diode Laser Technology XVII*, vol. 10900, pp. 121–126, SPIE, 2019.

[37] M. Malyj and J. Griffiths, "Stokes/anti-stokes raman vibrational temperatures: reference materials, standard lamps, and spectrophotometric calibrations," *Applied Spectroscopy*, vol. 37, no. 4, pp. 315–333, 1983.

[38] J. Christofferson, K. Maize, Y. Ezzahri, J. Shabani, X. Wang, and A. Shakouri, "Microscale and nanoscale thermal characterization techniques," *Electronic packaging*, 2008.

[39] W. Liu and B. Yang, "Thermography techniques for integrated circuits and semiconductor devices," *Sensor Review*, vol. 27, no. 4, pp. 298–309, 2007.

[40] P. Kolodner and J. A. Tyson, "Microscopic fluorescent imaging of surface temperature profiles with 0.01 c resolution," *Applied Physics Letters*, vol. 40, no. 9, pp. 782–784, 1982.

[41] P. Kolodner and J. A. Tyson, "Remote thermal imaging with 0.7-μm spatial resolution using temperature-dependent fluorescent thin flims," *Applied Physics Letters*, vol. 42, no. 1, pp. 117–119, 1983.

[42] A. Majumdar, J. Lai, M. Chandrachood, O. Nakabeppu, Y. Wu, and Z. Shi, "Thermal imaging by atomic force microscopy using thermocouple cantilever probes," *Review of Scientific Instruments*, vol. 66, no. 6, pp. 3584–3592, 1995.

[43] J. Christofferson and A. Shakouri, "Thermoreflectance based thermal microscope," *Review of Scientific Instruments*, vol. 76, no. 2, p. 024903, 2005.

[44] M. Farzaneh, K. Maize, D. Lüerßen, J. Summers, P. Mayer, P. Raad, K. Pipe, A. Shakouri, R. Ram, and J. A. Hudgings, "Ccd-based thermoreflectance microscopy: principles and applications," *Journal of Physics D: Applied Physics*, vol. 42, no. 14, p. 143001, 2009.

[45] P.-W. E. P.-W. Epperlein, "Micro-temperature measurements on semiconductor laser mirrors by reflectance modulation: A newly developed technique for laser characterization," *Japanese journal of applied physics*, vol. 32, no. 12R, p. 5514, 1993.

[46] P. K. Chan, K. P. Pipe, J. Plant, R. Swint, and P. Juodawlkis, “Temperature mapping and thermal lensing in large-mode, high-power laser diodes,” *Applied physics letters*, vol. 89, no. 20, p. 201110, 2006.

[47] P. Piva, R. Goldberg, I. Mitchell, S. Fafard, M. Dion, M. Buchanan, S. Charbonneau, G. Hillier, and C. Miner, “Reduced 980 nm laser facet absorption by band gap shifted extended cavities,” *Journal of Vacuum Science & Technology B: Microelectronics and Nanometer Structures Processing, Measurement, and Phenomena*, vol. 16, no. 4, pp. 1790–1793, 1998.

[48] P. Epperlein, G. Bona, and P. Roentgen, “Local mirror temperatures of red-emitting (al) gainp quantum-well laser diodes by raman scattering and reflectance modulation measurements,” *Applied physics letters*, vol. 60, no. 6, pp. 680–682, 1992.

[49] P. M. Mayer, D. Lüerßen, R. J. Ram, and J. A. Hudgings, “Theoretical and experimental investigation of the thermal resolution and dynamic range of ccd-based thermoreflectance imaging,” *JOSA A*, vol. 24, no. 4, pp. 1156–1163, 2007.

[50] P. Epperlein, “Basic diode laser engineering principles,” *Semiconductor Laser Engineering, Reliability and Diagnostics*, pp. 3–100, 2013.

[51] Y. Liu, G. Yang, Z. Wang, T. Li, S. Tang, Y. Zhao, Y. Lan, and A. Demir, “High-power operation and lateral divergence angle reduction of broad-area laser diodes at 976 nm,” *Optics & Laser Technology*, vol. 141, p. 107145, 2021.

[52] Y. Lan, G. Yang, Y. Liu, Y. Zhao, Z. Wang, T. Li, and A. Demir, “808 nm broad-area laser diodes designed for high efficiency at high-temperature operation,” *Semiconductor Science and Technology*, vol. 36, no. 10, p. 105012, 2021.

[53] T. Chen, L. Eng, Y. Zhuang, and A. Yariv, “Experimental determination of transparency current density and estimation of the threshold current of

semiconductor quantum well lasers," *Applied physics letters*, vol. 56, no. 11, pp. 1002–1004, 1990.

[54] X. Liu, M. H. Hu, H. K. Nguyen, C. G. Caneau, M. H. Rasmussen, R. W. Davis, and C.-E. Zah, "Comparison between epi-down and epi-up bonded high-power single-mode 980-nm semiconductor lasers," *IEEE Transactions on Advanced Packaging*, vol. 27, no. 4, pp. 640–646, 2004.

Appendix A

Code

The following code is used in the image processing step, as described in section 2.3. First, the thermoreflectance images of the LD facet are collected. Then, we get the average of all of them to decrease the image noise, in which more than a thousand images are collected to get high-quality images. The position is selected to compare and adjust Hot and Cold images to each other to find the amount of shift between them. Finally, we obtain the facet temperature of each position by using the thermoreflectance equation.

```
clc;
close all;
workspace;
format compact;
kappa=1/0.000245;
smooth_y=4;
smooth_x=2;
%% IMPORT DATA
hot0=dlmread('C:\Users\R.G\Desktop\1A\data\hot.txt','\t');
cold0=dlmread('C:\Users\R.G\Desktop\1A\data\cold.txt','\t');
flat1=dlmread('C:\Users\R.G\Desktop\1A\data\flat hot.txt','\t');
flat2=dlmread('C:\Users\R.G\Desktop\1A\data\flat cold.txt','\t');
```

```
dark1=dlmread('C:\Users\R.G\Desktop\1A\data\dark hot.txt','\t');
dark2=dlmread('C:\Users\R.G\Desktop\1A\data\dark cold.txt','\t');

dark=(dark1+dark2)./2;
flat=(flat1+flat2)./2;
%% DATA CHECK
%% hot vs cold
% imshow(mat2gray(hot0));
% pause(1)
% imshow(mat2gray(cold0));
%%dark field
% imshow(mat2gray(dark1-dark2));
% imshow(mat2gray(dark1));
% %%flat field
% imshow(mat2gray(flat1-flat2));
% mean(mean(flat1-flat2));
% imshow(mat2gray(flat1));
%% CHECK FOR SATURATION
sat=sum(sum(hot0>3900));
%% FLAT FIELD CORRECTION
flat=flat-dark;
imshow(mat2gray(flat));
gain=flat./imgaussfilt(flat,100);
imshow(mat2gray(gain));
%% BAD PIXELS
thresh=10;
imshow(mat2gray(gain))
f=fitdist(gain(:),'Normal');
% fixednoise=fixednoise;
bad=(gain<f.mu-thresh*f.sigma)|(gain>f.mu+thresh*f.sigma);
% bad=medfilt2(bad);
bad=imdilate(bad,strel("disk",8));
% Now fix the bad points in the gain
```

```
gain(bad)=f.mu;
imshow(mat2gray(gain));
%% APPLY Flat Field Correction
hot0=(hot0-dark)./gain;
cold0=(cold0-dark)./gain;
%% ILLUMINATION CORRECTION (BETTER NOT TO USE)
% illum=imgaussfilt((hot0+cold0)/2,400);
% imshow(mat2gray(illum))
% hot0=hot0./illum;
% cold0=cold0./illum;
%% SMOOTHING FILTER
h = fspecial('motion', 3, 0);
hot0=imfilter(hot0,h);
cold0=imfilter(cold0,h);
imshow(mat2gray(hot0))
%% CROP (choose the area to compare)
[~, rect] = imcrop(insertText(mat2gray(hot0),[0,0],
'SELECT REGION TO ALIGN, THEN RIGHT CLICK->CROP','FontSize',18));
hot= imcrop(mat2gray(hot0),rect);
cold= imcrop(mat2gray(cold0),rect);
bad= imcrop(mat2gray(bad),rect);
%% FIND THE SHIFT BETWEEN IMAGES
[x, y] = meshgrid(1:size(hot,2), 1:size(hot,1));
clear tlist
shf=0:0.005:0.1;
%shf=0.2
for i=1:length(shf)
fixedHot = interp2(hot.*~bad, x, y+shf(i),'makima');
fixedDiff=fixedHot-cold;
fixedAvg=(fixedHot+cold)./2;
temperature=kappa*fixedDiff./fixedAvg;
tlist(i,:)= mean((~bad.*temperature)');
end
```

```
pc=surf(1:size(tlist,2),shf,tlist);shading flat;view(2);
caxis([0 5]);colormap(jet);colorbar;
%find minimum negative
tlistn=tlist.*(tlist<0);
[~,ind]= max(sum(tlistn,2));
bestshf=shf(ind);
[x, y] = meshgrid(1:size(hot0,2), 1:size(hot0,1));
fixedHot = interp2(hot0, x, y+bestshf,'spline');
fixedDiff=fixedHot-cold0;
fixedAvg=(fixedHot+cold0)./2;
temperature=kappa*fixedDiff./fixedAvg;
temperature=temperature+24;
smoothDiff=medfilt2(fixedDiff);
pc=surf(flip(imrotate(medfilt2(temperature,[smooth_y smooth_x]),0)));
shading flat;view(2)
caxis([20 70]);
colorbar;
log(abs(sum(sum(fixedDiff<0))))

figure
tp=imrotate(temperature,0);
tp=tp(520:1200,600:1000);
T=mean(tp');
plot(T)
xlabel('distance from surface')
ylabel('temperature')
```